Title

Scaling a Dpp Morphogen Gradient through Feedback Control of Receptors and Co-receptors.

Journal

Developmental cell, 53(6)

ISSN

1534-5807

Authors

Zhu, Yilun
Qiu, Yuchi
Chen, Weitao
et al.

Publication Date

2020-06-01

DOI

10.1016/j.devcel.2020.05.029

Peer reviewed

Article

Developmental Cell

Scaling a Dpp Morphogen Gradient through Feedback Control of Receptors and Co-receptors

Graphical Abstract

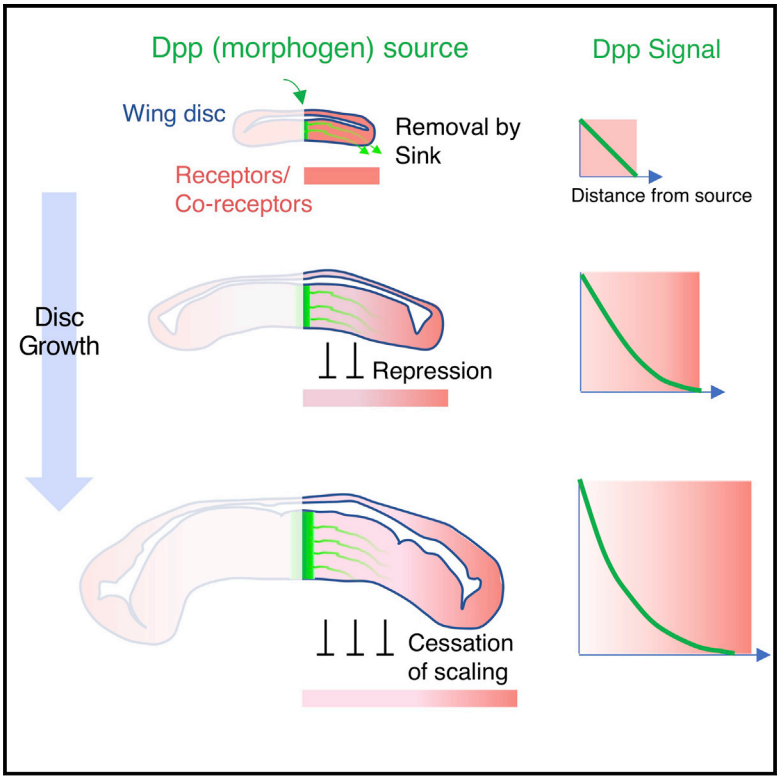

Authors

Yilun Zhu, Yuchi Qiu, Weitao Chen, Qing Nie, Arthur D. Lander

Correspondence

adlander@uci.edu

In Brief

Zhu et al. investigate how a morphogen gradient expands to fit a growing domain. They argue that initial boundary conditions, tissue growth, and feedback downregulation of receptor and co-receptor expression together create a positional information system that scales automatically, yet transiently.

Highlights

- The Dpp morphogen gradient of the *Drosophila* wing disc scales with disc size
- Feedback downregulation of receptors and co-receptors is required for gradient scaling
- A mathematical model shows how moving boundaries, growth, and feedback work together
- The secreted expander Pentagone does not spread sufficiently to explain scaling

Zhu et al., 2020, Developmental Cell *53*, 724–739
June 22, 2020
https://doi.org/10.1016/j.devcel.2020.05.029

CellPress

CellPress

Developmental Cell

Article

Scaling a Dpp Morphogen Gradient through Feedback Control of Receptors and Co-receptors

Yilun Zhu,[1,4] Yuchi Qiu,[2] Weitao Chen,[6,7] Qing Nie,[1,2,3,4,5] and Arthur D. Lander[1,3,4,5,8,*]
[1]Department of Developmental and Cell Biology, University of California Irvine, Irvine, CA 92697, USA
[2]Department of Mathematics, University of California Irvine, Irvine, CA 92697, USA
[3]Department of Biomedical Engineering, University of California Irvine, Irvine, CA 92697, USA
[4]Center for Complex Biological Systems, University of California Irvine, Irvine, CA 92697, USA
[5]NSF-Simons Center for Multiscale Cell Fate Research, University of California Irvine, Irvine, CA 92697, USA
[6]Department of Mathematics, University of California, Riverside, CA 92521, USA
[7]Interdisciplinary Center for Quantitative Modeling in Biology, University of California, Riverside, CA 92521, USA
[8]Lead Contact
*Correspondence: adlander@uci.edu
https://doi.org/10.1016/j.devcel.2020.05.029

SUMMARY

Gradients of decapentaplegic (Dpp) pattern *Drosophila* wing imaginal discs, establishing gene expression boundaries at specific locations. As discs grow, Dpp gradients expand, keeping relative boundary positions approximately stationary. Such scaling fails in mutants for *Pentagone* (*pent*), a gene repressed by Dpp that encodes a diffusible protein that expands Dpp gradients. Although these properties fit a recent mathematical model of automatic gradient scaling, that model requires an expander that spreads with minimal loss throughout a morphogen field. Here, we show that Pent's actions are confined to within just a few cell diameters of its site of synthesis and can be phenocopied by manipulating non-diffusible Pent targets strictly within the Pent expression domain. Using genetics and mathematical modeling, we develop an alternative model of scaling driven by feedback downregulation of Dpp receptors and co-receptors. Among the model's predictions is a size beyond which scaling fails—something we observe directly in wing discs.

INTRODUCTION

During development, gradients of secreted morphogens convey positional information, enabling cells to behave and differentiate according to their locations. Over a century of evidence suggests that positional information is often specified in relative coordinates, i.e., scaled to the territory being patterned (Cooke, 1981; De Robertis, 2006; Driesch, 1891; Inomata, 2017; Ishimatsu et al., 2018; Teleman and Cohen, 2000). Fifty years ago, Wolpert argued that this implies that morphogen gradients adjust themselves to the fields on which they act (Wolpert, 1969), a phenomenon that was eventually observed directly (Ben-Zvi et al., 2011b; Gregor et al., 2005; Hamaratoglu et al., 2011; Teleman and Cohen, 2000; Wartlick et al., 2011).

Wolpert noted that one type of gradient—a linear diffusion gradient from a source to an absorbing sink—scales naturally, automatically readjusting its slope whenever the sink moves (Wolpert, 1969). Over time, the idea that morphogens form simple source-sink gradients gave way to the view—supported by observations (e.g., Eldar et al., 2002; Entchev et al., 2000; Gregor et al., 2007; Teleman and Cohen, 2000)—that gradients are shaped by continual decay throughout the morphogen field. Gradients shaped in this way should not scale automatically, implying that other mechanisms must enable scaling. Progress toward identifying such mechanisms has been slow but received a boost with the development of the expansion-repression (ER) model (Ben-Zvi and Barkai, 2010), in which a morphogen represses the expression of a secreted "expander," which, by diffusing back toward the morphogen source, promotes morphogen spread. This mechanism is homeostatic—moving a distal field boundary away from a morphogen source increases production of the expander, which spreads the morphogen gradient toward the field boundary—and, if the expander is long lived, approximates "integral negative feedback," a control strategy that achieves perfect compensation (Ben-Zvi and Barkai, 2010).

So far, the ER model has been used to explain how gradients of bone morphogenetic proteins (BMPs) scale in response to embryo manipulations (Ben-Zvi et al., 2008) and during growth of larval wing imaginal discs (Ben-Zvi et al., 2011a). In the latter case, the relevant BMP is decapentaplegic (Dpp), which is produced by a stripe of cells in the center of the disc and spreads bidirectionally through the columnar epithelium to create gradients in the anterior and posterior compartments. During the larval period, wing discs grow at least 60-fold in anteroposterior dimension, and the Dpp gradient scales with it (Hamaratoglu et al., 2011; Wartlick et al., 2011). Support for the ER model in this setting was provided by the identification of a putative expander, the secreted protein Pentagone (Pent, also known as Magu). *Pent* is repressed by Dpp, restricting *Pent* to the

most lateral cells of the central wing pouch. Loss of *pent* dramatically shrinks the Dpp signaling gradient, and *pent* overexpression expands it (Vuilleumier et al., 2010). Moreover, in the absence of *pent*, developmental scaling of the Dpp gradient is greatly impaired (Ben-Zvi et al., 2011a; Hamaratoglu et al., 2011). Although Pent's mechanism of action is not fully understood, it binds heparan sulfate proteoglycans (HSPGs) and triggers their removal from the cell surface. The same HSPGs act as co-receptors for BMPs (Kuo et al., 2010), including Dpp (Fujise et al., 2001; Jackson et al., 1997), strongly suggesting that Pent expands Dpp gradients by inhibiting receptor-mediated Dpp uptake.

Here, we re-examine the role of Pent in the *Drosophila* wing disc, focusing on an important requirement of the ER model, namely that the expander spread in a nearly uniform manner over the morphogen field. Spreading uniformly is not the same as merely being diffusible, as spread quantifies the balance between transport (e.g., diffusion) and decay, where decay means all processes that remove a substance from a diffusing pool (i.e., destruction, uptake, and leakage out of the system). In a stable diffusion gradient, a common measure of spread is the "apparent decay length," or λ_{app}, the distance over which concentration falls by a factor of 1/*e* (Lander et al., 2009). In the ER model, if an expander's λ_{app} is not greater than the size of the morphogen field, the expander will affect the morphogen differently at different locations, and effective scaling will not occur.

As described below, we found λ_{app} for Pent to be very small, strongly suggesting that Dpp gradient scaling cannot rely on Pent to play the expander role required by the ER model. Through genetic experiments and mathematical modeling, we arrived at an alternative model, in which the feedback that drives scaling is not repression of an expander but morphogen-mediated regulation of receptor (and co-receptor) function, a phenomenon that is fairly common in patterning systems (e.g., Cadigan et al., 1998; Fujise et al., 2003; Kähkönen et al., 2018; Lecuit and Cohen, 1998). A key feature of this model is that it is dynamic, terminating scaling at a size that depends on the parameters of the system. In view of evidence that a growing Dpp gradient itself participates in driving disc growth (Wartlick et al., 2011), this feature suggests ways in which bi-directional coupling between patterning and growth could be achieved.

RESULTS

Quantifying Morphogen Gradient Scaling

For discrete pattern elements, such as gene expression boundaries, one can define scaling as the preservation of these elements' relative positions. During development, however, sharp gene expression boundaries may emerge only late (del Alamo Rodríguez et al., 2004; Oliveira et al., 2014) or read out morphogen signals in indirect (e.g., time-integrated) ways (e.g., Balaskas et al., 2012; Dessaud et al., 2007; Nahmad and Stathopoulos, 2009). To investigate developmental scaling directly, it is thus important to monitor morphogen gradients themselves or gradients of immediate downstream signals (e.g., phosphorylated Mad [pMad], in the case of Dpp). As smooth gradients lack landmarks with which to assess relative position, this means tracking the locations of constant gradient amplitudes over time. It can be challenging, however, to measure absolute concentration in tissues. Furthermore, absolute morphogen or signaling molecule concentration may not even be the best readout of positional information across developmental time, because changing characteristics of cells likely influence how they decode morphogen signals. In wing discs, for example, changes in cell dimensions between first larval instar and the end of disc growth (Widmann and Dahmann, 2009) imply that cell volumes increase by at least 7-fold.

For these reasons, morphogen gradient scaling is often evaluated in terms of preservation of relative gradient shape, typically quantified by the degree to which the apparent decay length (λ_{app}) of the morphogen (or its downstream signaling intermediates) changes proportionately with size of the morphogen field (e.g., Wartlick et al., 2011). For gradients of exponential shape, λ_{app} is simply the constant λ in the formula $C = C_0 e^{-x/\lambda}$, where C is concentration, x is distance from the morphogen source, and C_0 is the value of C at $x = 0$. In practice, λ_{app} is often measured as the distance over which a gradient falls to 1/*e* of its starting value (or by extracting the length constant from a best-fit exponential curve). Here, we follow others in using λ_{app} as a first-line metric for assessing scaling, but also take care to visually analyze absolute gradient shapes whenever possible. As we argue below, changes in both gradient amplitude and shape may play an important role in enabling certain kinds of scaling mechanisms.

Evaluating Pentagone as an "Expander" in Morphogen Gradient Scaling

The ER model of scaling requires an expander to spread uniformly across a morphogen field, i.e., traverse it without much decrement in concentration. Although Pent can be detected at a distance from its site of synthesis (Norman et al., 2016; Vuilleumier et al., 2010), and when overexpressed in the posterior half of the disc can influence gradient shapes in the adjacent anterior (Vuilleumier et al., 2010), such observations do not speak to how steeply Pent concentrations decline over distance.

To address this, we first selectively knocked down *pent* in the posterior compartment of the disc. We reasoned that, if Pent truly diffuses freely across the disc, then both sides of the disc must be fed by both the anterior and posterior sources of the molecule. Thus, the extent to which strong phenotypes from knocking down Pent in one compartment were observed in both compartments would provide a measure of how uniformly Pent spreads.

We used compartment-specific drivers to express *pent*-directed RNAis exclusively in the posterior and, as a positive control, a disc-wide driver to express RNAi everywhere. Effects on the Dpp signaling gradient were scored as changes to λ_{app} of pMad. We observed that posterior knockdown of *pent* produced only posterior effects—equivalent to those of global knockdown—and no detectable anterior effects (Figure 1). This implies that Pent decay is sufficiently strong, over distance, that at best a small fraction of Pent made in the posterior reaches the anterior. The alternative explanation that there is some barrier to Pent diffusion at the midline can be dismissed given the ease with which overexpressed Pent in the (entire) posterior compartment can produce phenotypes in the anterior (Vuilleumier et al., 2010).

If Pent concentrations decay over distance, then Pent should form gradients. To visualize these, we took several approaches.

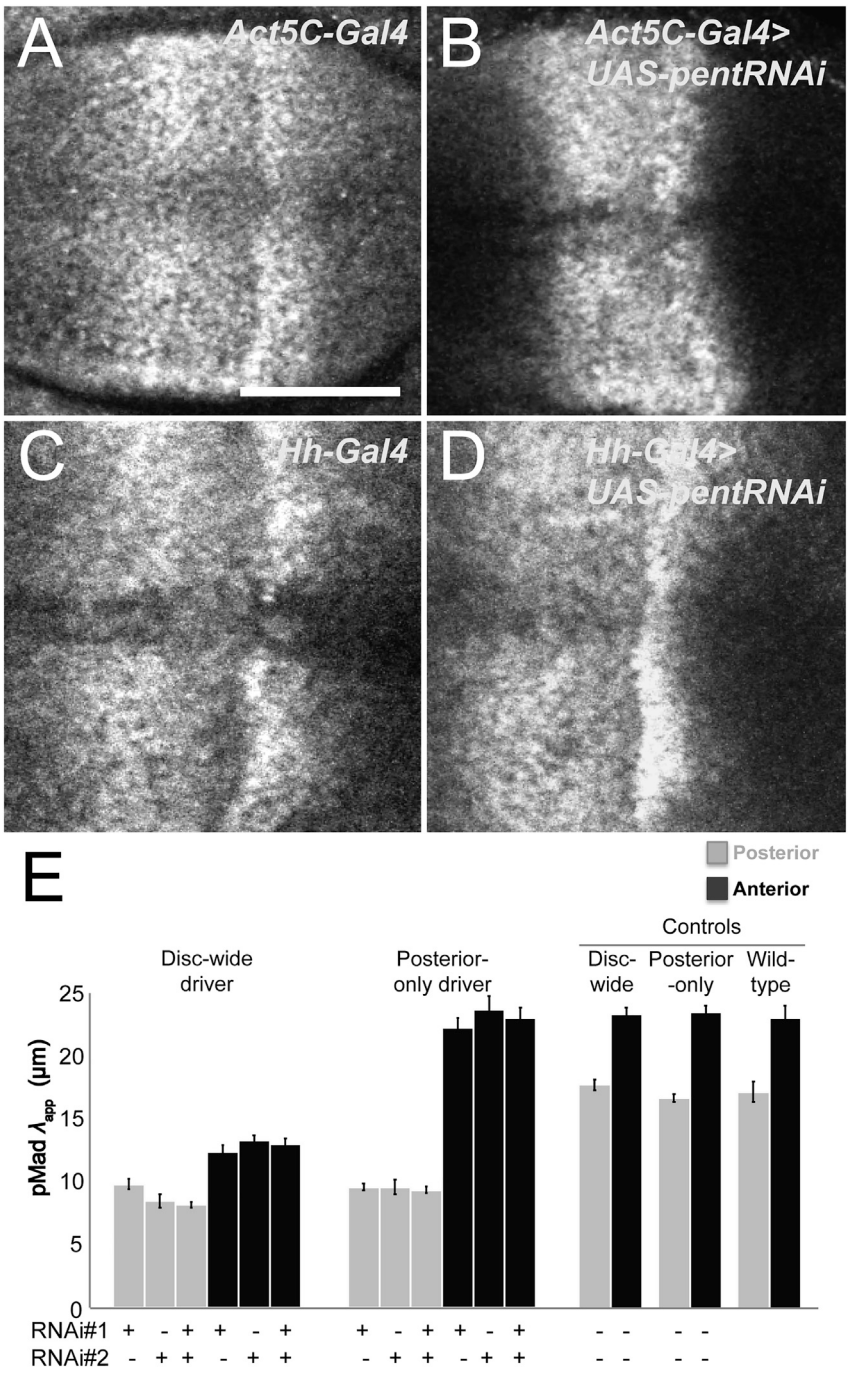

Figure 1. The Effect of Pent on the Dpp Signaling Gradient Is Compartment Specific

(A–D) Phospho-Mad (pMad) staining of *Act5C-Gal4* (A), *Act5C-Gal4>UAS-pentRNAi* (B), *hh-Gal4* (C), and *hh-Gal4>UAS-pentRNAi* (D) third instar wing discs. Expressing *pentRNAi* (either of two different RNAi sequences) disc wide (with *Act5C-Gal4*), shrinks the pMad gradient in both anterior and posterior compartments, whereas limiting *pentRNAi* to the posterior compartment (with *hh-Gal4*) affects only the posterior compartment. Bar represents 50 μm. Anterior is to the left and posterior to the right.

(E) Results are summarized as changes in pMad apparent decay length (λ_{app}) in each compartment for each of the four genotypes in (A–D). n varies between 12 and 23 for each condition. Error bars = SEM.

We first used green fluorescent protein-tagged Pent (GFP-Pent), which we verified complements a *pent* mutation (Figure S1), and expressed it in wing discs under the control of various *Gal4* drivers (Figures 2A–2C′ and S1D–S1K). In all cases, fluorescence declined dramatically away from sites of expression. Fitting to an exponential function yielded estimates of λ_{app} on the order of 6–8 μm. (Figures 2D and S1D–S1G). A low level of diffuse signal was also seen over longer distances (Figures S1D′–S1F′), similar to that noted in others' observations using a differently tagged form of Pent (Vuilleumier et al., 2010).

Since it is possible that the diffusion or decay of Pent could have been affected by fusion to GFP, we also carried out experiments that did not require tagging the molecule: we expressed wild-type *pent* in mosaic clones in wing discs. Levels of Pent made by such clones were similar to those in *pent*'s normal region of synthesis (Figure S2F). As shown in Figure 3, *pent* overexpression clones are associated with two phenomena: reduced pMad staining (Figures 3A–3E′) and reduced immunostaining for the cell-surface HSPG Dally-like protein (Dlp) (Figures 3F–3I′). As discussed above, Pent binds to (Vuilleumier et al., 2010) and drives the internalization of both Dlp and the related HSPG Dally (Norman et al., 2016), so the observed loss of Dlp in response to Pent expression agrees with previous studies. The reduction in pMad staining, although not previously reported, is likely a consequence of the same process, since Dally and Dlp act as co-receptors for Dpp signaling, and their elimination in clones has been shown to produce cell-autonomous decreases in pMad (Belenkaya et al., 2004; Fujise et al., 2003).

Notably, in the clones in Figure 3, the effect of *pent* overexpression on pMad and Dlp can be detected only for short distances away from clonal boundaries. A precise decay length is difficult to calculate, as pMad and Dlp patterns are already spatially non-uniform, but the data in Figure 3N, in which we combine clonal marking with GFP, visualization of Pent using an antibody to the native protein, and staining for Dlp, suggest that Pent acts on Dlp over a range of about 5–10 μm, similar to the λ_{app} estimated using GFP-Pent (Figure 2). We conclude that, although Pent is diffusible, it decays strongly with distance. This suggests Pent acts relatively locally, rather than globally, undermining support for the ER model as an explanation for Dpp gradient scaling.

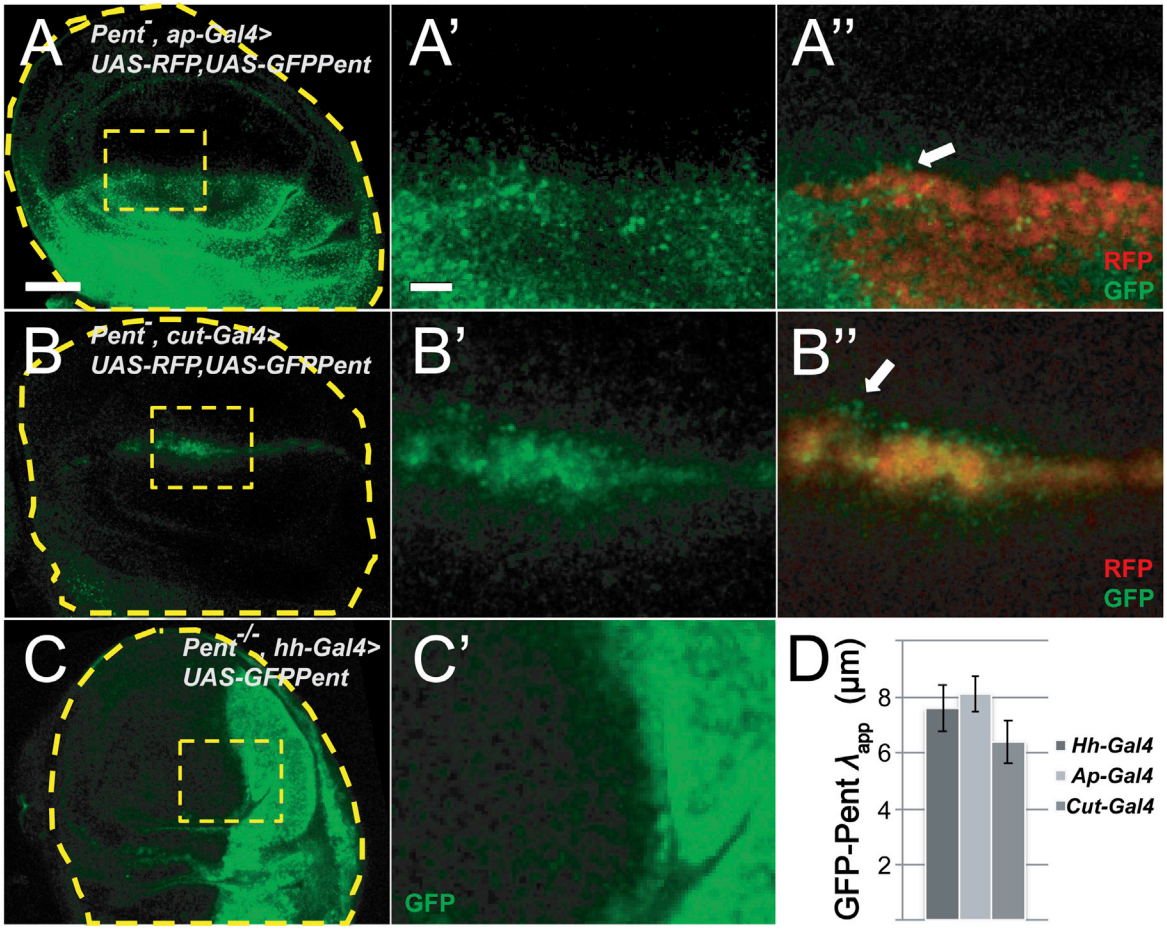

Figure 2. The Apparent Decay Length (λ_{app}) of GFP-Pent Is Short

(A–C) *UAS-GFP-Pent* expression was driven by *ap-Gal4* (dorsal domain, A–A″); *cut-Gal4* (dorsal-ventral boundary, B–B″); and *hh-Gal4* (posterior compartment, C–C′). With *ap-Gal4* and *cut-Gal4*, *UAS-RFP* marked GFP-Pent-producing cells (A″ and B″). Arrows show GFP fluorescence a few cell diameters away from RFP-expressing cells. With *hh-Gal4*, both endogenous *pent* alleles were mutant to show that the spread of GFP-Pent is similar whether or not all or only some Pent molecules were GFP labeled. Bar in (A) represents 50 μm and applies to (A, B, and C). Bar in A′ represents 10 μm and applies to (A′, A″, B′, B″, and C′).
(D) Values of λ_{app} for GFP-Pent were determined for the genotypes in A–C; numbers of discs analyzed were 17 for *ap*-Gal4; 14 for *cut*-Gal4, and 10 for *hh*-Gal4. Error bars = SEM.

Scaling of the Dpp Signaling Gradient Is a Transient Phenomenon

Before investigating alternative explanations for scaling, we more closely examined scaling dynamics. We collected many wild-type wing discs, spanning a range of sizes, and calculated λ_{app} for pMad, using the same measurement approaches taken by other investigators, making an effort to avoid various pitfalls and artifacts (e.g., measuring too close to the dorsoventral boundary; Hamaratoglu et al., 2011).

Our observations (Figures 4, 5, and S3) confirm that λ_{app} grows roughly in proportion to disc size but also show that it does so only up to the time (part-way through third larval instar) that posterior compartment sizes reach ~50–60 μm—about a fourth to a third of their final size, or about two cell cycles (approximately one day) prior to the end of disc growth. After that, scaling seems to cease rather abruptly. Such behavior has not been noted previously, possibly because other groups have focused more on documenting the existence of scaling during most of disc growth, rather than on how it behaves during the very last stages of growth. What this behavior suggests is that whatever mechanism accounts for scaling of the Dpp gradient, it is size (or time) limited, i.e., has a maximal distance or duration over which it functions. Thus, the challenge in explaining scaling in the wing disc is not only to understand how it happens but also to understand why it stops when it does.

Pent Function Can Be Mimicked by Cell-Autonomously Disabling Co-receptors at the Edges of the Dpp Morphogen Field

The evidence that Pent does not spread far (Figures 1, 2, and 3) raises the question of whether, to carry out its function, Pent needs to spread at all. One way to address this might be to physically tether Pent so that it cannot move. A simpler approach is to test whether Pent function can be mimicked by replicating the actions of Pent in a purely cell-autonomous way in the domain in which Pent is produced. As discussed above, current

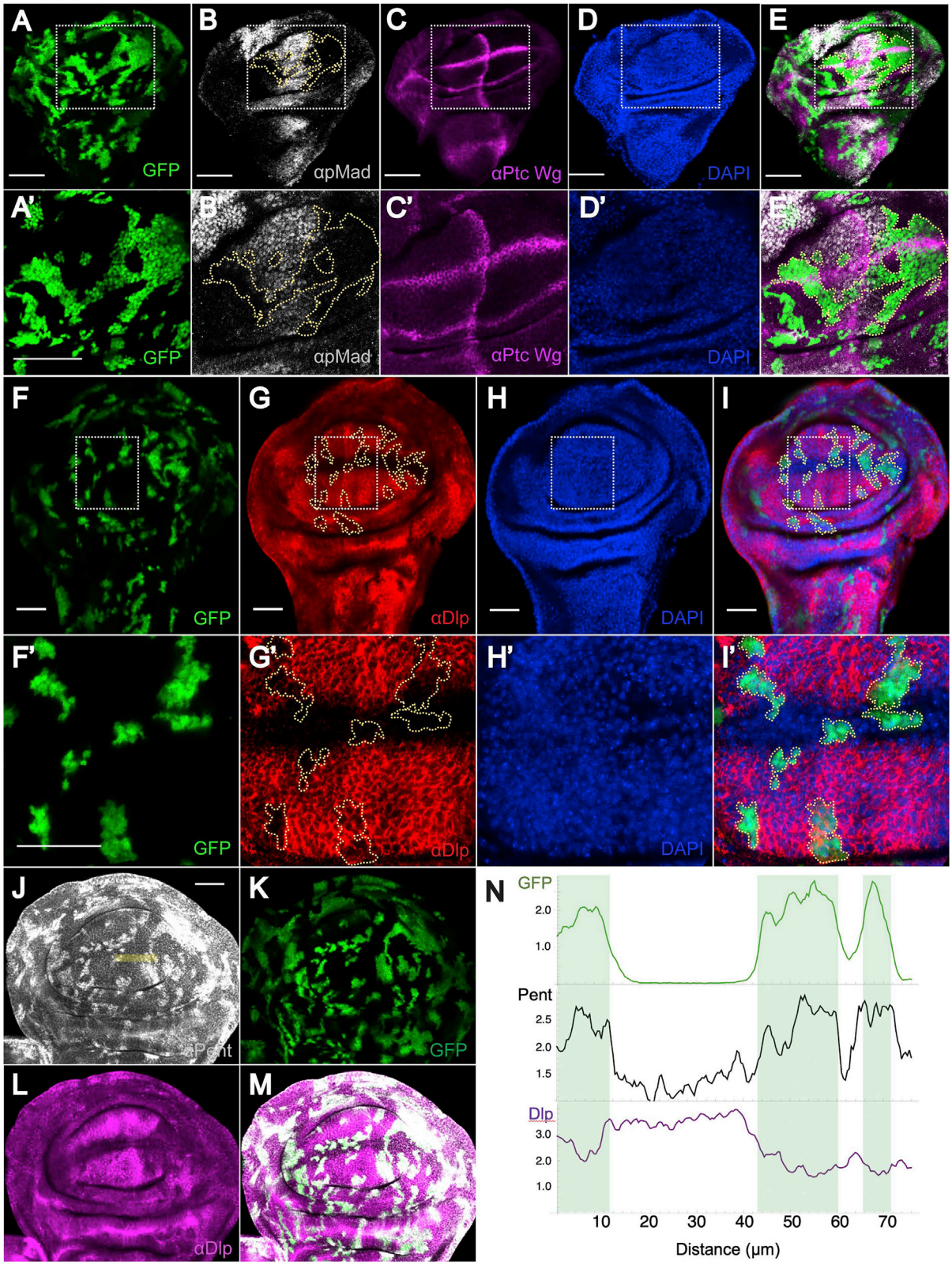

Figure 3. Pent Overexpression Has Only Local Effects

(A–E′) Third instar wing disc with clones of cells overexpressing *pent* (GFP, green; A, A') stained with anti-pMad (gray; B, B'), anti-Ptc and anti-Wg antibodies (magenta; C, C'), DAPI (blue; D, D'), and as a merged image (E, E'). Ptc/Wg staining marks the anteroposterior (A/P) and dorsoventral (D/V) boundaries, as well as

(legend continued on next page)

consensus is that Pent acts by reducing levels (and thereby function) of HSPG co-receptors, in so doing decreasing Dpp uptake and increasing Dpp spread. We gathered several additional observations consistent with that view: for example, in *pent* mutants the Dpp gradient (not just the pMad gradient) shrinks (Figures S4A and S4B), there is no change in Dpp diffusivity in *pent* mutant discs (by fluorescence correlation spectroscopy) (Figures S4C–S4F), and there appears to be no significant direct interaction between Pent and the Dpp receptor Tkv (by cross-correlation raster scanning intensity correlation microscopy, a test for molecular co-diffusion; Figures S4G–S4I).

To reduce HSPG function in a cell-autonomous way, we used *sulfateless-RNAi* (*sfl-RNAi*). *Sfl* encodes an enzyme required for N-sulfation, and consequently the function, of HSPGs (Baeg et al., 2001; Lin and Perrimon, 1999). We compared pMad gradients in the posterior compartment of wing discs in which either *sfl*-RNAi, *tkv*-RNAi, *pent*, or *GFP* were placed under the control of *brk-Gal4*, which drives expression in a domain very similar to that of *pent* (Figures 4A–4E). Additional experiments using *ds-Gal4*, which also drives expression in a similar domain, yielded similar results (Figures S5A–S5E). We collected data from >60 discs per genotype and plotted pMad decay length against compartment size (Figure 4F). To quantify changes in scaling over time, we fit data to a function that switches smoothly from one linear slope to another (both the slopes and the switching point were fit to the data).

As expected, the value of λ_{app} for *brk-Gal4>UAS-Pent* gradients was larger, at comparable disc sizes, than in control discs (*brk-Gal4>UAS-GFP*), showing that adding Pent in its own expression domain expands the Dpp gradient. Interestingly, *brk-Gal4>UAS-sflRNAi* gradients were similarly expanded, although not quite as much. This was seen in small discs undergoing scaling (posterior compartment sizes of 10–50 μm) and large discs in which scaling had already slowed or stopped. We also noticed that adult wing phenotypes of *brk Gal4>UAS-sflRNAi* flies resembled those of *brk Gal4>UAS-Pent* flies (Figures S5F–S5I).

These results argue that impairing HSPG function where *pent* is expressed can phenocopy *pent* overexpression. Consistent with the view that the role of HSPGs is to enhance receptor-mediated Dpp uptake, we also find that knocking down receptor expression in the *brk* domain has the same effect on the pMad gradient as disrupting HSPG function in the same domain (Figures 4E and 4F).

Interestingly, if we express *sflRNAi* throughout the entire disc (using *Act5C-Gal4*), the Dpp gradient shrinks (Figure 4D′), implying that the expansion we saw with *brk-Gal4>UAS-sflRNAi* (Figure 4) and *ds-Gal4>UAS-sflRNAi* (Figure S5) could not have been an artifact of "leaky" expression in the central part of the disc, as that should have produced the opposite result.

These experiments also argue against a model in which Pent-mediated internalization of HSPGs does not actually destroy these molecules but releases them as shed forms that diffuse away, acting as long-range expanders of the Dpp gradient. In fact, many cells do shed HSPGs of the family that includes Dally and Dlp (Bernfield et al., 1999; Ishihara et al., 1987); shed forms have been proposed to play a role in morphogen gradient formation (Giráldez et al., 2002), and a truncated, soluble form of Dally, when expressed in wing discs, can both diffuse widely and expand Dpp gradients (Takeo et al., 2005). But if this model were correct, eliminating HSPG function in the periphery of the wing disc should have contracted, not expanded, Dpp gradients, as we observed.

Feedback Regulation of Receptors and Co-receptors Is Required for Scaling

One reason that λ_{app} is widely used as a measure of morphogen gradient shape is that a simple model, the "uniform-decay" model, connects it to the biophysics of gradient formation: if morphogen decay is uniform in space, and the morphogen field is sufficiently large (and sufficiently one-dimensional), then steady-state gradient shape should have the form $e^{-x/\lambda}$, with $\lambda = \lambda_{app} = \sqrt{D/k}$, where D is the morphogen diffusion coefficient, and k is a rate constant of morphogen removal (e.g., uptake) (Lander et al., 2009).

In general, one cannot assume that morphogen decay is uniform in space because morphogens may influence their own uptake or destruction. Some (e.g., Wingless and Hedgehog in *Drosophila* wing discs) upregulate their own removal, such "self-enhanced decay" characteristically alters gradient shape (Eldar et al., 2003; Lander et al., 2009). In contrast, Dpp downregulates both its receptor Tkv (through indirect effects on *tkv* transcription; Lecuit and Cohen, 1998) and the HSPG co-receptor Dally (Fujise et al., 2003). As Tkv appears to be the major determinant of Dpp uptake and, thereby removal (Akiyama et al., 2008; Lecuit and Cohen, 1998), and Dally likely boosts this function of Tkv, and may even mediate some uptake itself (Fujise et al., 2003), we expect Dpp gradients to be shaped by "self-repressed decay."

Although the effects of self-enhanced and self-repressed decay on steady-state gradient shape are fairly subtle (Lander et al., 2009), these processes can have large effects on how gradients respond to perturbations. For example, self-enhanced decay gradients display increased robustness to changes in amplitude (i.e., threshold locations do not move nearly as much as they do in uniform-decay gradients; Eldar et al., 2003). Self-repressed decay gradients, it turns out, display enhanced sensitivity to changes in the size of the morphogen field, a phenomenon that—as we will see shortly—can drive morphogen gradient scaling.

the Dpp production region. (A′–E′) are enlargements of rectangles in (A–E). pMad staining is reduced within the clones (outlined area in B and B′) but only barely so outside their boundaries. The image shows one representative disc of five analyzed.
(F–I′) A wing disc containing clones of cells overexpressing *pent* (marked with GFP, green; F, F′) stained with anti-Dlp antibody (G, G′), DAPI (H, H′), and as a merged image (I, I′). (F′–I′) are enlargements of the rectangles in (F–I). Dlp staining is markedly reduced within the clones (outlined areas in G and G′) but with little obvious change outside clone boundaries. The image shows one representative disc of nine analyzed.
(J–M) Representative wing disc with clones of cells overexpressing *pent* (marked with GFP, green; K) stained with anti-Pent (J), anti-Dlp antibodies (L), and as a merged image (M). Shown is one representative disc of eight analyzed.
(N) Profiles of GFP, Pent, and Dlp, extracted along the yellow line in (J), are plotted (background fluorescence, estimated from Figure S2D, was subtracted from the anti-Pent signal). Green boxes mark the boundaries of *pent* overexpression clones. Bars represent 50 μm.

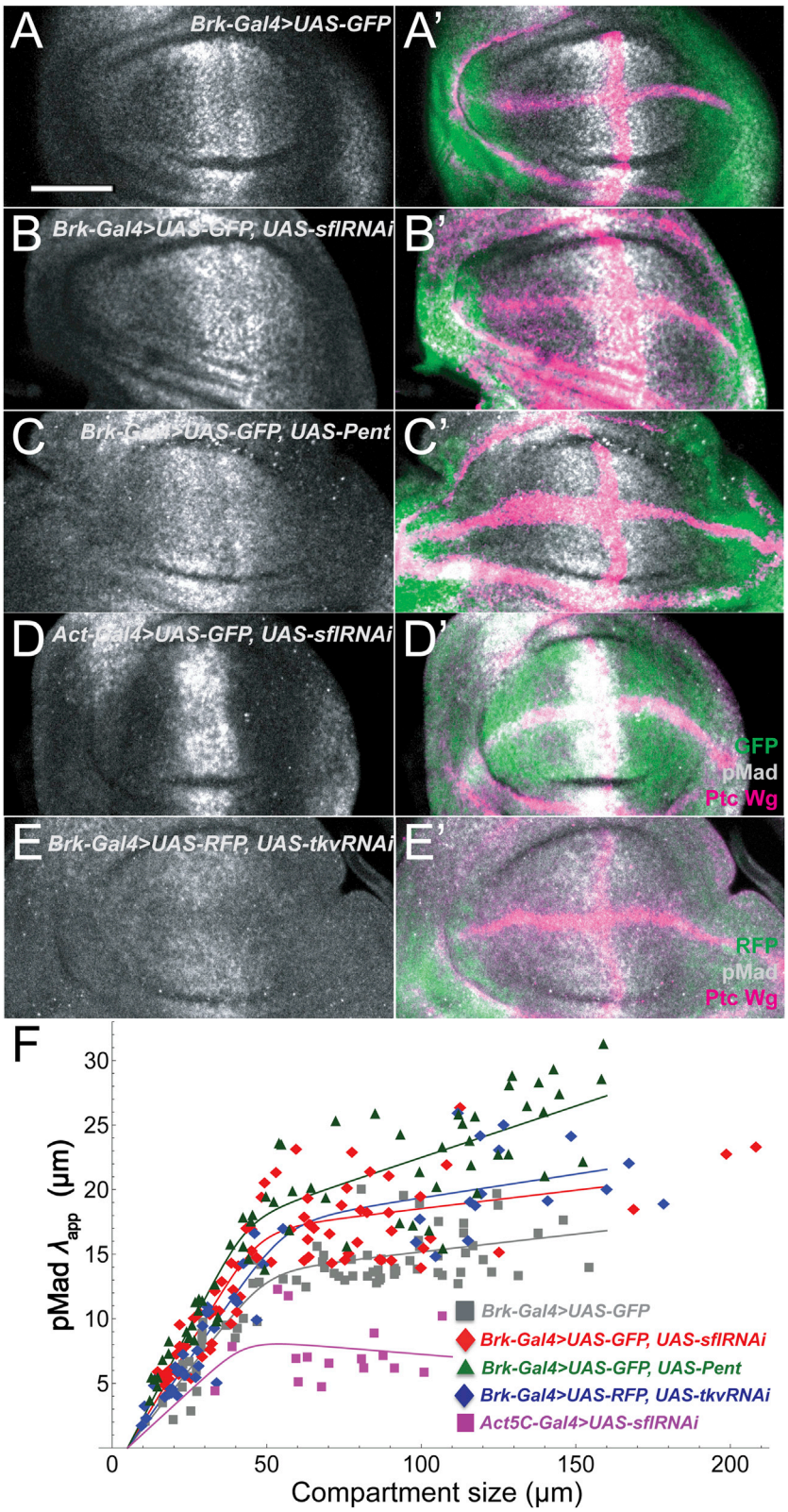

Figure 4. Local Inhibition of Co-receptor or Receptor Function Phenocopies *pent* Overexpression

(A–E′) *brk-Gal4*, which drives expression in a domain similar to that of *pent*, was used to express *UAS-GFP* (negative control, A–A′); *UAS-GFP; UAS-sflRNAi* (inhibition of HSPG sulfation B–B′); *UAS-GFP; UAS-Pent* (*pent* overexpression, C–C′); and *UAS-RFP; UAS-tkvRNAi* (inhibition of receptor expression, E–E′). In addition, *Act5C-Gal4* was used to drive *UAS-GFP; UAS-sflRNAi* throughout the disc (D–D′). Scale bar, 50 μm.

(F) λ_{app} for pMad in the posterior compartments of wing discs of all five genotypes, determined for discs of different sizes, was plotted against compartment size. Data are fit to smooth curves as described (see STAR Methods). n = 71, 74, 65, 16, and 49 for the genotypes in (A, B, C, D, and E), respectively.

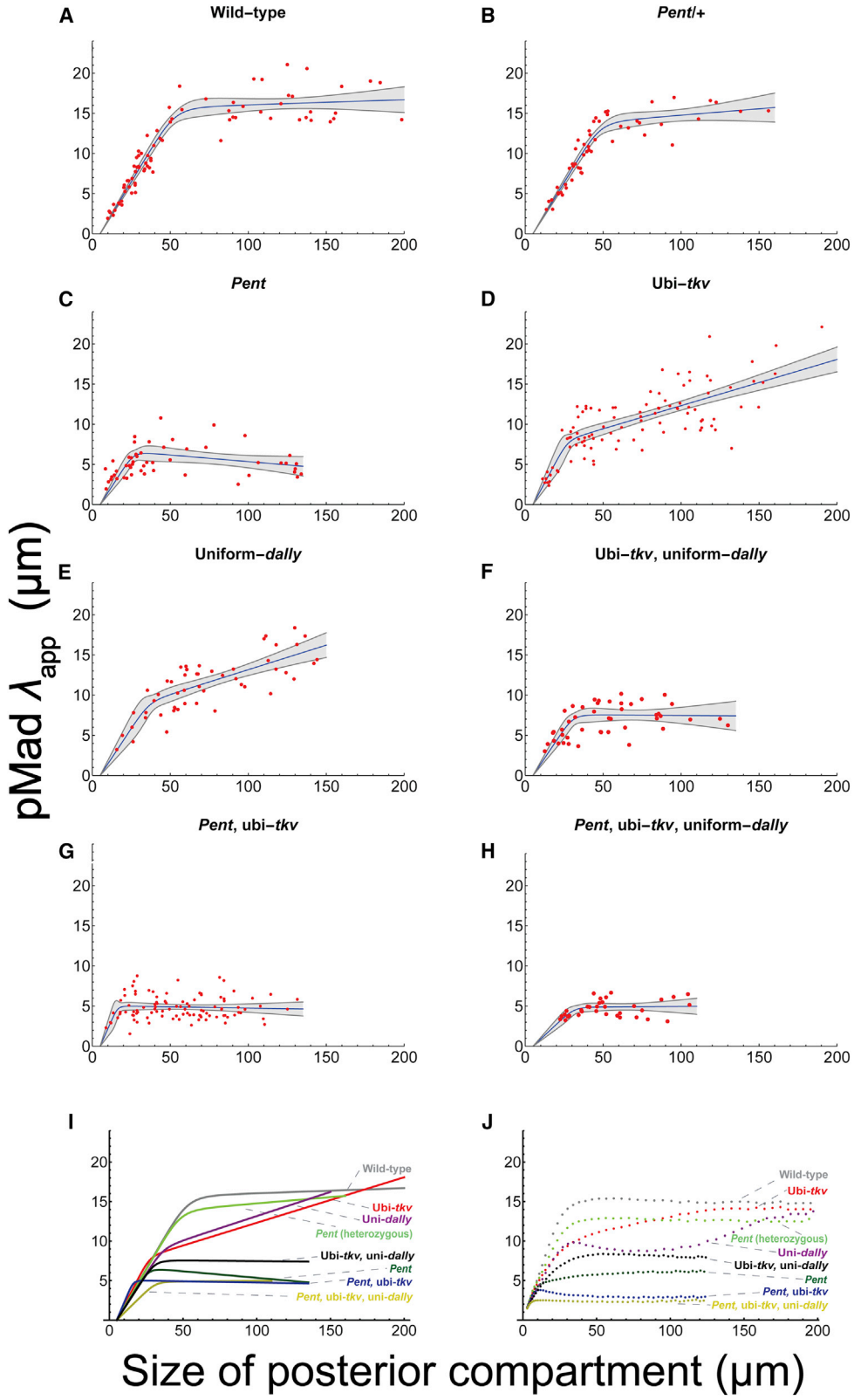

Figure 5. Feedback Regulation of *tkv* and *dally* Is Required for Scaling

(A–H) pMad apparent decay lengths in the wing disc posterior compartment were measured and fit as in Figure 4. Envelopes around curves represent 95% confidence intervals for the fits. Genotypes were (A) wild type; (B) $+/pent^{2}$; (C) $pent^{2}/pent^{2}$; (D) tkv^{Df}/tkv^{strII}; *ubi-tkv-HA*; (E) *Act5C-Gal4, dally*^{80}*/UAS-dally, dally*^{80};

(legend continued on next page)

Before discussing the theory behind this assertion, we present experimental evidence in support of it: to test whether self-repression of decay is required for Dpp gradient scaling in the wing disc, it was necessary to disable the feedback loops that allow Dpp to downregulate *tkv* and *dally*. For *tkv*, we used a transgenic allele in which a ubiquitin promoter drives ubiquitous, unregulated expression of HA-tagged *tkv* (Ogiso et al., 2011). When combined with null mutation of the endogenous *tkv* locus, viable flies are obtained, with late-third larval instar wing discs that do not differ significantly in pattern from wild type, except for the fact that *tkv* expression is spatially uniform, rather than graded. We refer to this genotype as "Ubi-*tkv*." To disable feedback on *dally*, we used an *Act5C-Gal4* driver to drive a *UAS-dally* transgene in a uniform pattern in a *dally*-mutant background ($dally^{80}/dally^{80}$). We refer to this genotype as "Uniform-*dally*."

Figure 5 shows results for a large number of wild-type; *pent*; $pent^{+/-}$; Ubi-*tkv*; Uniform-*dally*; Ubi-*tkv plus*Uniform-*dally*; *pent plus* Ubi-*tkv*; and *pent* plus Ubi-*tkv* plus Uniform-*dally* discs of a broad range of sizes. λ_{app} was measured for pMad gradients and plotted against posterior compartment sizes. Curves were fit as in Figure 4F, allowing the size at which scaling behavior slows or stops to be estimated independently for each dataset.

The results show that scaling is significantly impaired when either *tkv* or *dally* regulation is bypassed and nearly eliminated when both are bypassed. These differences emerge mainly after posterior compartments grow beyond 30 μm. Above that size, Ubi-*tkv* and Uniform-*dally* continue to scale but much more slowly than wild-type gradients. Eventually, however, such gradients do "catch up" to wild-type gradients, as a result of the fact that wild-type gradients cease scaling sooner. In contrast, doubly mutant Ubi-*tkv*/Uniform-*dally* gradients stop expanding altogether once posterior compartments grow beyond about 30 μm, reaching a final λ_{app} about half that of wild type.

The defect in Ubi-*tkv*/Uniform-*dally* gradients is almost, but not quite, as severe as that in *pent* mutants, which cease scaling at a slightly earlier size. Interestingly, the phenotype of *pent*/Ubi-*tkv* and *pent*/Ubi-*tkv*/Uniform-*dally* discs was only slightly more severe than for *pent* alone. These results support the conclusion that both scaling, and the effect of Pent on scaling, depend upon feedback regulation of *tkv* and *dally* by Dpp.

Modeling the Dynamics and Endpoints of Scaling

To explain the behaviors in Figure 5, we turned to mathematical modeling. Accounting for all the cell biological phenomena that affect Dpp gradient shape requires modeling a large number of molecular species and processes. As many of these processes are not quantitatively understood, they were represented as simply as possible, with model behaviors explored over parameter ranges that were wide but plausible (given available data). The goal was not so much to identify parameter values as to determine whether existing observations can be matched without invoking additional mechanisms. To the extent that inclusion of new mechanisms is not required, models such as these can help identify which processes potentially play the most important roles in morphogen gradient scaling.

The molecular species represented in the model are Dpp, Tkv, "co-receptor" (to represent both Dally and Dlp), Pent, Dpp-co-receptor complexes, and two types of Dpp receptor complexes (the more stable of which forms with the aid of co-receptor-mediated catalysis; Kuo et al., 2010), plus pMad and Brk. An additional transcription factor is included downstream of the transcriptional repressor Brk to enable it to activate Tkv and co-receptor synthesis indirectly (the role of this factor in the model resembles that of *optomotor blind*; del Alamo Rodríguez et al., 2004). Dpp and Pent are the only diffusing species, with Pent being assigned the same diffusivity as that measured empirically for Dpp (Zhou et al., 2012). Details of modeling and parameter selection are presented in STAR Methods.

Summary results for multiple genotypes are shown in Figure 5J, with detailed simulations in Figures 6 and S9. The behaviors of the genotypes in Figure 5I are reasonably well replicated: initially, all modeled genotypes scale well, until posterior compartment sizes reach ~10 μm. Up to this time, Dpp and pMad gradient shapes produced by the model are essentially straight lines from source to the end of the morphogen field (Figure 6).

Automatically adjusting straight-line gradients call to mind the "source-sink" scaling mechanism of (Wolpert, 1969), which exemplifies what mathematicians call a "boundary-layer effect," whereby phenomena at a boundary influence gradient shape at a distance. For steady-state diffusion gradients, the approximate distance over which boundary-layer effects occur is the *intrinsic decay length*, $\lambda_{intrinsic}$, defined as the square root of the ratio of the diffusion coefficient and the (effective) removal rate constant.

As previously noted, for uniform-decay gradients on a sufficiently large one-dimensional field, gradient shape is described by $e^{-x/\lambda}$, with $\lambda = \lambda_{app} = \sqrt{D/k}$; thus, for such gradients $\lambda_{app} = \lambda_{intrinsic}$. But "sufficiently large field" here turns out to mean large compared with $\lambda_{intrinsic}$. With fields smaller than $\lambda_{intrinsic}$, gradient shape becomes less exponential and more linear; the more linear the gradient, the farther into it boundary-layer effects will occur. Wolpert's source-sink gradients are merely the limiting case of $\lambda_{intrinsic} = \infty$, (no decay within the morphogen field), yielding straight-line gradients that scale perfectly with boundary movement. As long as morphogen gradients operate in a regime of large $\lambda_{intrinsic}$ (compared with morphogen field size), they too will scale automatically (this is also true in higher dimensions—see section in STAR Methods). However, this can only go on for so long, as field size should eventually catch up with $\lambda_{intrinsic}$—at which point gradients will become more exponential and scaling will stop.

In the mathematical model, scaling initially displayed by all genotypes stops at different sizes (in agreement with experimental observations; Figure 5I), for reasons that depend on the genotype. We consider first the wild type: in that situation, the initial

(F) tkv^{strII}/tkv^{a12}, *ubi-tkv-HA; Act5C-Gal4,* $dally^{80}/$*UAS-dally,* $dally^{80}$; (G) $pent^{2}$, $tkv^{Df}/pent^{A17}$, tkv^{strII}; *ubi-tkv-HA*; and (H) $pent^{A17}$,$tkv^{strII}/pent^{2}$, tkv^{a12}, *ubi-tkv-HA; Act5C-Gal4,* $dally^{80}/$*UAS-dally,* $dally^{80}$.

(I) Summary of results in (A–H). n = 78, 53, 52, 100, 52, 45, 100, and 34 for the genotypes in (A), (B), (C), (D), (E), (F), (G), and (H), respectively.

(J) Data from mathematical modeling (see STAR Methods; Figure 6) showing the evolution of the pMad apparent decay length over time.

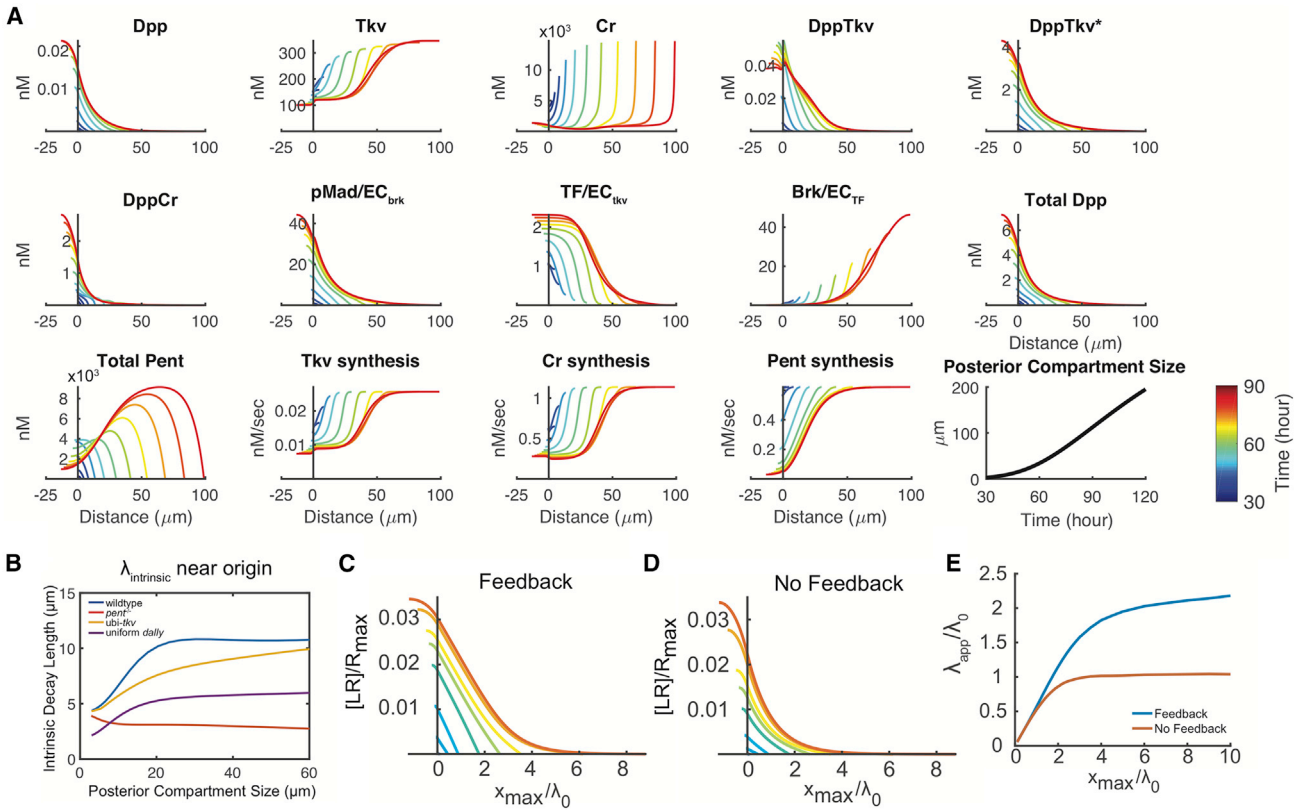

Figure 6. Modeling Dpp Gradient Scaling in the Posterior Compartment of the Wing Disc

(A) Time evolution of the wild-type Dpp morphogen gradient. Graphs show distributions of free Dpp, Dpp receptor and co-receptor complexes, and downstream signals and targets, simulated as described in STAR Methods. $x = 0$ represents the anteroposterior compartment boundary. The final graph in the simulation shows the growth of the posterior compartment over time, and the legend shows how time is represented by color in each of the graphs. Simulations for other genotypes are shown in the Figure S9.

(B) The source-adjacent Dpp intrinsic decay length ($\lambda_{intrinsic}$ averaged over locations from $x = 0$ to $x = 0.1\ x_{max}$) for four genotypes (wild type, *pent*$^{-/-}$, ubi-*tkv*, and uniform-*dally*) was calculated and plotted as a function of compartment size (x_{max}). $\lambda_{intrinsic}$ captures the distance over which boundary effects occur, so that source-adjacent $\lambda_{intrinsic}/x_{max}$ provides a measure of the extent to which a gradient's shape near the morphogen source is strongly boundary controlled. Transient rises in $\lambda_{intrinsic}$ demonstrate the effects of feedback downregulation of *tkv* and *dally*.

(C–E) The principle of pseudo-source-sink scaling illustrated with a simplified, steady-state model, with only four free parameters, which includes only ligands, receptors, and ligand-receptor complexes, irreversible capture of ligands by receptors, and downregulation of receptor synthesis. Values of *LR* (ligand-receptor complexes) are normalized to R_{max} (receptor concentration obtained in the absence of ligand binding or feedback) and plotted against compartment size normalized to the intrinsic decay length that would be observed in the absence of ligand binding or feedback (λ_0). (C) illustrates the effect of feedback downregulation of receptor production; in (D) feedback is turned off and ligand production rate adjusted to produce a similar value of LR near $x = 0$. (E) summarizes the apparent decay lengths (λ_{app}), relative to λ_0, for the curves in (C–D). Notice how, with feedback, the *LR* gradient achieves a much longer period of scaling. For further explanation and parameter space exploration see STAR Methods.

value of $\lambda_{intrinsic}$ (~5 μm everywhere) suggests that scaling should fail sooner than it does but, as the disc grows, the value of $\lambda_{intrinsic}$ near the morphogen source rises (Figure 6B), extending the period of scaling. The reason for the rise is that receptors and co-receptors become increasingly downregulated (since they are the primary means of morphogen removal, their loss drives $\lambda_{intrinsic}$ up). Interestingly, to prolong scaling it is not necessary for $\lambda_{intrinsic}$ to grow as fast as the disc itself. This is because once strongly non-uniform expression of receptors and co-receptors sets in—low near the morphogen source and high far away—the actual sink at the far end of the morphogen field becomes less and less important. Instead, the territory with high receptor/co-receptor expression itself acts like a sink, due to the high level of morphogen uptake there. We call this behavior "pseudo-source-sink" scaling, as it emulates a boundary-layer effect without the need for a true tissue boundary (Figures 6C–6E).

The phenomenon that drives pseudo-source-sink scaling is, fundamentally, amplitude growth: in other words, it is because Dpp and pMad levels at the start of the gradient rise with disc growth that receptor and co-receptor expression become increasingly repressed, and at greater distance, over time. Whereas true source-sink scaling reflects a direct coupling of field size to gradient scale, pseudo-source-sink scaling depends on indirect feedback: changes in field size first produce changes in gradient amplitude, and these then drive changes in gradient scale.

Why should changes in field size cause changes in amplitude? In the model, several processes contribute. The simplest is that the production region itself grows with the disc; as it does, it

feeds more Dpp into the gradient (the magnitude of the effect depending on the level of morphogen decay within the production region). A second reason arises from the laws of physics and the fact that the gradient has already been scaling: according to Fick's first law, net diffusive flux at any point is proportional to the slope of the diffusion gradient. So, whenever a gradient expands by becoming shallower, diffusive flux at the origin must decrease. That in turn leaves more molecules available to contribute to the local concentration of morphogen, raising free morphogen concentration.

Two other mechanisms can also contribute to amplitude growth but have minor effects in the model: to the extent that Dpp molecules associated with or internalized within cells are very long lived, the Dpp signal that cells receive will lag significantly behind the free Dpp concentration; this can cause pMad levels to rise even after Dpp levels have leveled off. And to the extent that disc growth is not purely exponential but rather slows as time goes on (Wartlick et al., 2011), the loss of Dpp and pMad due to dilution will diminish, ultimately raising Dpp and pMad concentration.

Does amplitude growth, as seen in the model, actually happen *in vivo*? Monitoring Dpp and pMad amplitudes over time is challenging, not only because of individual variation among discs but also because discs change dramatically in thickness as they grow, necessitating corrections for systematic changes in the efficiency of immunostaining and/or imaging. Nonetheless, groups that have made such measurements consistently report amplitude growth in the wing disc Dpp gradient, although the degree to which they observe it varies (Hamaratoglu et al., 2011; Wartlick et al., 2011). The model parameters used in Figures 5 and 6 predict an approximately 7-fold increase in Dpp and 12-fold increase in pMad over the time that posterior compartments lengthen ~20-fold (from 10 to 195 μm; Figure 6), but the actual changes are likely less important than the degree to which they decrease Tkv and co-receptor expression.

To investigate the dynamics of that decrease *in vivo*, we monitored expression of a *tkv* enhancer trap line over a range of disc sizes. As shown in Figure S7F, the pattern of *tkv* expression in early, small discs is much more uniform than it is later, strongly implying that Dpp-mediated repression is minimal early on and builds gradually. Similarly, Widmann and Dahmann (2009) find that *brk* expression is also fairly uniform in early discs, only becoming strongly suppressed by Dpp later. We see much the same thing with *pent* which, like *brk*, is a direct target of Dpp signaling: early expression in the center of the wing pouch, with the pattern of exclusively peripheral expression only emerging later (Figure S7L). These results are all consistent with a Dpp signaling gradient that grows in amplitude over time.

Given that feedback regulation of receptors and co-receptors plays an essential role in prolonging scaling in the mathematical model, it is not surprising that genotypes that eliminate both feedback loops stop scaling much earlier (at a posterior compartment size of ~20 μm). In contrast, if only a single feedback loop is eliminated, gradients expand for a bit longer (posterior compartment size ~30 μm), then very gradually catch up to a final λ_{app} almost equal to wild type (this agrees with experimental observations; Figure 5). Examination of the model suggests an explanation for this behavior: because a single feedback loop capable of adjusting $\lambda_{intrinsic}$ remains, pseudo-source-sink scaling persists (Figure 6B), but the slower pace at which it happens means that one of the factors that contributes to amplitude growth (decreased diffusive flux due to shallower gradient slope) is less pronounced, leading to slower scaling.

In the model, scaling also fails for *pent* mutant discs, but the reasons are somewhat different. In the model, and as we observed experimentally (Figure S7), *pent* is expressed throughout the wing pouch at early times. Since Pent removes co-receptors, Pent loss means increased co-receptor function, driving down $\lambda_{intrinsic}$ in most or all of the disc, and causing source-sink scaling to fail prematurely. Thus, whereas elimination of feedback control of receptors and co-receptors impedes scaling by interfering with the process of scaling itself, elimination of Pent further impedes scaling by changing the initial conditions of the disc. Consistent with this view are the results of RNAi up- and down-shift experiments (Figure 7), which suggest that the effects of Pent on gradient scale are, to a fairly substantial degree, due to actions that occur during early disc growth (i.e., before mid-third instar).

In the model, the behaviors seen with other genotypes may be understood as combinations of the effects discussed above. Interestingly, the model captures the observed fact that *pent* mutant discs do not "catch up" after scaling slows, unlike Ubi-*tkv* and Uniform-*dally* discs. This difference only emerged in the model when we accounted for the fact that basal Brinker (*brk*) expression increases dramatically during disc growth (Hamaratoglu et al., 2011); without this, modeled *pent* discs also displayed "catch-up" behavior. In effect, Brinker's rise seems to act as a countervailing force to pseudo-source-sink scaling, pushing thresholds back toward the Dpp source at the same time that increased Dpp signaling pushes them farther away. As Hamaratoglu et al. (2011) point out, highest *brk* expression occurs where there is essentially no Dpp signaling, so Dpp itself cannot explain *brk*'s rise. In the model, we arbitrarily adjust *brk* amplitude to follow the findings of Hamaratoglu et al. (2011); however, it is intriguing to speculate that there could be some coupling between *brk* expression and disc size that would make such coupling automatic.

DISCUSSION

Morphogen gradients play a central role in animal development, tying cell behavior to spatial location. Whereas monotonic gradients of almost any sort can encode location, to encode "relative" location on a domain of changeable size, gradients must scale. To do so, at least one of three processes—morphogen production, transport, or removal (decay)—must somehow be coupled to the size of the morphogen field.

There have been several proposals for making such coupling automatic (Ben-Zvi and Barkai, 2010; Cheung et al., 2011; Wolpert, 1969), an elegant example of which is the ER model. This study began as an attempt to test whether the secreted protein Pent, which has been implicated in scaling of the *Drosophila* wing disc Dpp gradient, fits the requirements of the expander in this model. We found that Pent lacks the necessary spatial range, and that its effects can be phenocopied by disabling co-receptors in just the Pent expression domain (Figures 1, 2, 3, and 4), suggesting that Pent need not act at a distance. We

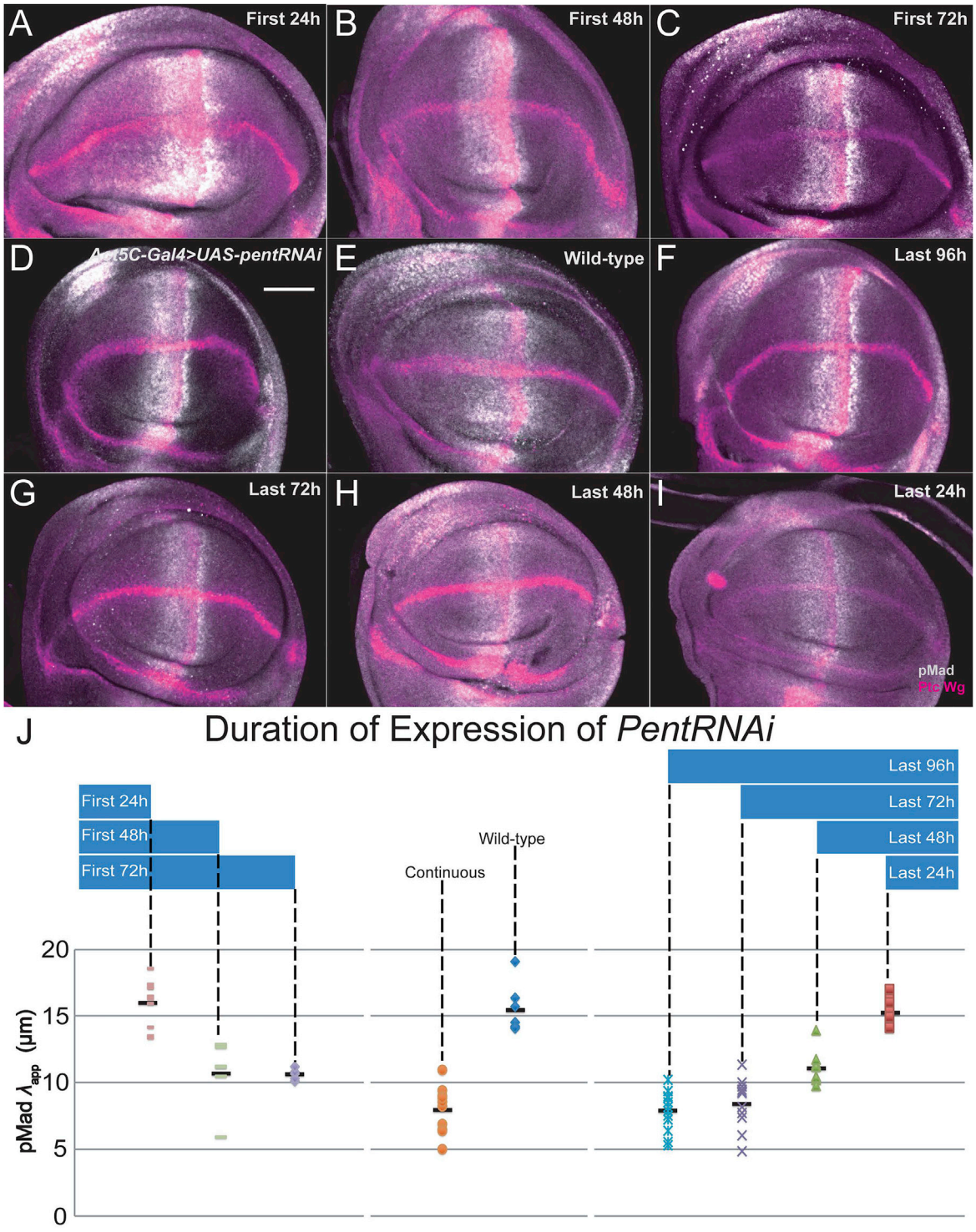

Figure 7. Temporal Requirement for Pent

The *Act5C-Gal4; tubP-Gal80^{ts}* system was used together with *pentRNAi* to achieve inducible or repressible knockdown of *pent* (see STAR Methods).

(A–I) Representative wing discs in which *pentRNAi* was either expressed continuously (D), not expressed (E), or expressed for defined time periods—24 (A), 48 (B), or 72 h after egg laying (C); or 96 (F), 72 (G), 48 (H), or 24 h (I) prior to wandering stage. Discs were stained with anti-pMad (gray) and mixed anti-Ptc and anti-Wg antibodies (magenta). Bar represents 50 μm.

(J) Comparison of pMad decay lengths in the posterior compartments of wing discs from the above larvae. n = 10, 6, 5, 10, 9, 12, 11, 10, and 10, for the genotypes in (A), (B), (C), (D), (E), (F), (G), (H), and (I), respectively. Black bars represent mean.

then made the observation that feedback repression of receptor and co-receptor synthesis is required for scaling (Figure 5).

How exactly does scaling happen? Having a mathematical model that reproduces wild-type and mutant phenotypes allowed us to develop a plausible explanation. Surprisingly, the explanation does not attribute scaling to a single mechanism but rather to a collection of passive and active processes.

First, when discs are very small—with compartment sizes up to about 10 μm, as one observes through early or mid-second larval instar—the model exhibits source-sink scaling because $\lambda_{intrinsic}$ is large enough that boundaries act as sinks. Although it is not possible to measure $\lambda_{intrinsic}$ directly, λ_{app} sets a lower bound on $\lambda_{intrinsic}$ and is well known at later stages (for both Dpp and pMad) to be on the order of 15–20 μm (Entchev et al., 2000; Hamaratoglu et al., 2011; Teleman and Cohen, 2000; Wartlick et al., 2011). It is thus reasonable to think that, at early times, $\lambda_{intrinsic}$ could indeed exceed morphogen field size.

Later, as discs grow beyond their initial values of $\lambda_{intrinsic}$, the model predicts a "pseudo-source-sink-scaling" regime (Figure 6), where rising morphogen levels drive down receptor and co-receptor expression, raising $\lambda_{intrinsic}$ near the morphogen source. Far from the morphogen source, however, $\lambda_{intrinsic}$ remains small, effectively creating a "pseudo-sink." As long as growth occurs in the amplitude of the morphogen gradient near the source, gradients respond by becoming shallower near the source, which makes them expand further outward. Moreover, as discussed above, when gradients become shallower, that in itself drives amplitudes up, effecting something of a positive feedback.

This process occurs until receptor and co-receptor expression can be downregulated no further—their levels cannot fall to zero because their function is required to drive their repression. After that, wild-type gradients outgrow their $\lambda_{intrinsic}$ and cease scaling altogether. Not surprisingly, genotypes that compromise the ability of the morphogen to repress receptor and/or co-receptor synthesis result in gradients that cease scaling sooner.

In the output of the mathematical model, the transition from a regime in which gradients scale to one in which they do not is marked by a shift in gradient shape from linear to roughly exponential (Figure 6). To some extent this behavior is an artifact of using on a one-dimensional formulation. Current evidence indicates that Dpp diffuses in the basolateral space between columnar cells of the disc (Harmansa et al., 2017; Zhou et al., 2012); as a result, one should expect a continual "leak" of Dpp through the adjacent basement membrane (such structures are not barriers to diffusion; Dowd et al., 1999), producing, in effect, an additional sink. A more complete analysis of source-sink scaling with sinks in multiple dimensions shows that, as long as cell height and disc width increase in size proportionately (which is approximately what occurs during larval growth), gradients will still scale automatically but may display any shape between linear and exponential (see STAR Methods). Furthermore, the necessary and sufficient condition for source-sink scaling—that $\lambda_{intrinsic}$ be larger than the anteroposterior field size—remains unchanged.

The idea that amplitude growth contributes substantially to morphogen gradient scaling is not new (reviewed by Umulis and Othmer [2013]). For example, selection for larger or smaller *Drosophila* embryos is accompanied by compensatory shifts in the locations at which Bicoid target genes are turned on. These shifts occur not because of a change in λ_{app} of the Bicoid gradient but an increase in gradient amplitude alone (Cheung et al., 2011). For exponential gradients (like the Bicoid gradient), simple amplitude increase produces constant-distance shifts in threshold positions, making thresholds near the morphogen source over-scale and those far away under-scale. Thus, like source-sink scaling, scaling due to pure-amplitude growth runs into spatial limits beyond which it is not very effective. The pseudo-source-sink mechanism partially compensates for this problem by displacing the effective sink away from the source as the amplitude near the source grows. However, it should be noted that in this case, what is truly scaling is just the relative shape of the morphogen gradient, as measured by its λ_{app}, and not the locations where absolute thresholds are crossed. At least some Dpp target genes (e.g., *dad*) do seem to scale in just this way (Hamaratoglu et al., 2011; Wartlick et al., 2011).

In addition to the various mechanisms—source-sink scaling, amplitude growth, and pseudo-source-sink scaling—that drive Dpp gradient expansion in the model described here, other processes may matter *in vivo*. Growth itself tends to propel forward the molecules within a tissue—a process termed "advection"—and some growth-driven gradient expansion can occur by that process alone, although under typical conditions the effect is likely to be small (Fried and Iber, 2014). Automatic scaling of certain locations within morphogen gradients can also occur if gradients operate far from steady state, i.e., if growth moves cells to new locations faster than the dynamic processes that determine gradient shape can adjust (Fried and Iber, 2014). The model we present here, at least over the parameter ranges explored, operates fairly close to steady state (i.e., gradients are relatively independent of growth rate), meaning that such "dynamics"-dependent scaling is not a significant contributor.

Overall, the experiments and modeling presented here suggest a view of scaling as more "kluge" than elegant control system. Small fields with leaky boundaries contribute source-sink and amplitude growth scaling effectively "for free," but not indefinitely, as both start to fail at large field size. Pseudo-source-sink effects prolong scaling, but only for so long, as receptor function can be suppressed only so much before signaling itself becomes too compromised.

This study suggests that the source-sink gradients of early theorists (Wolpert, 1969), which fell strongly out of favor once it was observed that gradient shapes are quasi-exponential, may actually have much to offer in explaining the early behaviors of morphogen gradients. Interestingly, recent work argues that source-sink behavior is also the primary determinant of BMP gradient shape in early zebrafish embryos (Zinski et al., 2017). The behavior in that system would, by our nomenclature, be more precisely termed pseudo-source-sink, since the sink in that system arises from the binding of BMP to chordin, and chordin is downregulated by BMP—a feedback loop functionally analogous to the downregulation of Tkv and Dally by Dpp in the wing disc. The parallels between that system and the work described here are intriguing because the BMP gradient that patterns the early vertebrate embryo also exhibits scaling behavior (in response to embryo bisection [Ben-Zvi et al., 2008; De Robertis, 2006] as well as other kinds of manipulations [Huang and Umulis, 2019]).

The inherent limitations of pseudo-source-sink scaling that, in the model, cause scaling to stop once a certain size is reached may seem like a drawback but may actually be a feature. Morphogens control not only pattern but also growth; in wing discs this is an essential function of Dpp (Affolter and Basler, 2007; Martín-Castellanos and Edgar, 2002). Wartlick et al. argue that the key signal that maintains disc growth is a continual rising Dpp signal (Wartlick et al., 2011). If gradient scaling is required to ensure that this rise occurs proportionally at all locations, as is the case in the model, failure of scaling could potentially play a causal role in terminating growth. What is intriguing about this idea is that it predicts that the size at which growth stops should correlate with the size at which scaling stops, which we in fact observe in the data: as shown in Figure 5, Pent$^{-/-}$ and Ubi-*tkv*/Uniform-*dally* mutant discs stop growing at a substantially smaller size than wild-type discs. These observations suggest that it may be better to view scaling and growth as one coupled system, rather than a mechanism for adjusting pattern to size.

Although this study provides a potential explanation for Dpp gradient scaling that correctly predicts the larval phenotype of the *pent* mutant, it does not provide a satisfying explanation for why Pent is used by wing discs in the first place. In the model, *pent* discs fail to scale mainly because they start out with too small a $\lambda_{intrinsic}$, but since all Pent does (in the model) is inhibit receptor function, it is not clear why discs do not just dispense with Pent altogether and simply express fewer receptors and co-receptors from the outset. The situation suggests that there may be as-yet-unappreciated functions of Pent. For example, even though the model argues that Pent diffusion is not necessary for scaling, it might still be possible that Pent has a useful role as a repressible expander during very early stages, when Pent's λ_{app} is not so small, relative to disc size. It may also be worth recalling the characteristic adult phenotype displayed by *pent* mutants: loss of the fifth longitudinal vein (Vuilleumier et al., 2010). Whereas scaling abnormalities might explain mispositioning of a vein, vein loss suggests that some Pent actions may be unrelated to Dpp gradient scaling.

SUPPORTING CITATIONS

The following references appear in the Supplemental Information: Gibson and Perrimon, 2005; Lander et al., 2002

STAR★METHODS

Detailed methods are provided in the online version of this paper and include the following:

- KEY RESOURCES TABLE
- RESOURCE AVAILABILITY
  - Lead Contact
  - Materials Availability
  - Data and Code Availability
- EXPERIMENTAL MODEL AND SUBJECT DETAILS
  - Drosophila Stocks and Genetics
  - Detailed Genotypes
- METHOD DETAILS
  - Clonal Analysis
  - Egg-Laying Assay
  - Conditional Knockdown of *Pent*
  - Antibodies and Immunostaining
  - Imaging
  - Fluorescence Correlation Spectroscopy (FCS) and Cross-correlation Raster Image Correlation Spectroscopy (ccRICS)
  - Mathematical Modeling
  - Lagrangian Framework for Solving Mathematical Equations
  - Parameter Selection
  - Simulating Rescue by Compartment-wide Pent Overexpression; Evaluating the Necessity for Pent Diffusivity
  - A Reduced Model that Exhibits Pseudo-Source-Sink Behavior
  - The Influence of Dimensionality on Source-Sink Scaling
- QUANTIFICATION AND STATISTICAL ANALYSIS
  - Image Analysis
  - Fitting Scaling Dynamics

SUPPLEMENTAL INFORMATION

Supplemental Information can be found online at https://doi.org/10.1016/j.devcel.2020.05.029.

ACKNOWLEDGMENTS

We thank Giorgos Pyrowolakis, Tetsuya Tabata, Hiroshi Nakato, Avital Rodal, and Richard Mann for generously sharing strains and reagents. We also thank Giorgos Pyrowolakis and Stephen DiNardo for gifts of antibodies. Many thanks to Michelle Digman, Thomas Schilling, and Rahul Warrior for valuable comments and suggestions. Michelle Digman also provided assistance on FCS and ccRICS techniques. This work was funded by grants from the NIH (P50-GM076516), NSF (DMS1763272), and Simons Foundation (594598).

AUTHOR CONTRIBUTIONS

Conceptualization, Y.Z. and A.D.L.; Methodology, Y.Z., Y.Q., W.C., Q.N., and A.D.L.; Software, Y.Z., Y.Q., W.C., and A.D.L.; Formal Analysis, Y.Z., Y.Q., W.C., and A.D.L.; Investigation, Y.Z.; Resources, Q.N. and A.D.L.; Writing – Original Draft, Y.Z., Y.Q., and A.D.L.; Writing – Review & Editing, Y.Z., Y.Q., W.C., Q.N., and A.D.L.; Supervision, Q.N. and A.D.L.; Funding Acquisition, Q.N. and A.D.L.

DECLARATION OF INTERESTS

The authors declare no competing interests.

Received: October 29, 2019
Revised: March 23, 2020
Accepted: May 26, 2020
Published: June 22, 2020

REFERENCES

Affolter, M., and Basler, K. (2007). The decapentaplegic morphogen gradient: from pattern formation to growth regulation. Nat. Rev. Genet. *8*, 663–674.

Akiyama, T., Kamimura, K., Firkus, C., Takeo, S., Shimmi, O., and Nakato, H. (2008). Dally regulates Dpp morphogen gradient formation by stabilizing Dpp on the cell surface. Dev. Biol. *313*, 408–419.

Baeg, G.H., Lin, X., Khare, N., Baumgartner, S., and Perrimon, N. (2001). Heparan sulfate proteoglycans are critical for the organization of the extracellular distribution of Wingless. Development *128*, 87–94.

Balaskas, N., Ribeiro, A., Panovska, J., Dessaud, E., Sasai, N., Page, K.M., Briscoe, J., and Ribes, V. (2012). Gene regulatory logic for reading the Sonic Hedgehog signaling gradient in the vertebrate neural tube. Cell *148*, 273–284.

Belenkaya, T.Y., Han, C., Yan, D., Opoka, R.J., Khodoun, M., Liu, H., and Lin, X. (2004). Drosophila Dpp morphogen movement is independent of dynamin-mediated endocytosis but regulated by the glypican members of heparan sulfate proteoglycans. Cell *119*, 231–244.

Ben-Zvi, D., and Barkai, N. (2010). Scaling of morphogen gradients by an expansion-repression integral feedback control. Proc. Natl. Acad. Sci. USA *107*, 6924–6929.

Ben-Zvi, D., Pyrowolakis, G., Barkai, N., and Shilo, B.Z. (2011a). Expansion-repression mechanism for scaling the dpp activation gradient in Drosophila wing imaginal discs. Curr. Biol. *21*, 1391–1396.

Ben-Zvi, D., Shilo, B.Z., and Barkai, N. (2011b). Scaling of morphogen gradients. Curr. Opin. Genet. Dev. *21*, 704–710.

Ben-Zvi, D., Shilo, B.Z., Fainsod, A., and Barkai, N. (2008). Scaling of the BMP activation gradient in Xenopus embryos. Nature *453*, 1205–1211.

Bergman, T.L., Lavine, A.S., Inropera, F.P., and Dewitt, D.P. (2011). Fundamentals of Heat and Mass Transfer, Seventh Edition (John Wiley & Sons).

Bernfield, M., Götte, M., Park, P.W., Reizes, O., Fitzgerald, M.L., Lincecum, J., and Zako, M. (1999). Functions of cell surface heparan sulfate proteoglycans. Annu. Rev. Biochem. *68*, 729–777.

Cadigan, K.M., Fish, M.P., Rulifson, E.J., and Nusse, R. (1998). Wingless repression of Drosophila frizzled 2 expression shapes the Wingless morphogen gradient in the wing. Cell *93*, 767–777.

Cheung, D., Miles, C., Kreitman, M., and Ma, J. (2011). Scaling of the bicoid morphogen gradient by a volume-dependent production rate. Development *138*, 2741–2749.

Cooke, J. (1981). Scale of body pattern adjusts to available cell number in amphibian embryos. Nature *290*, 775–778.

De Robertis, E.M. (2006). Spemann's organizer and self-regulation in amphibian embryos. Nat. Rev. Mol. Cell Biol. *7*, 296–302.

del Alamo Rodríguez, D., Terriente Felix, J., and Díaz-Benjumea, F.J. (2004). The role of the T-box gene optomotor-blind in patterning the Drosophila wing. Dev. Biol. *268*, 481–492.

Deshpande, M., Feiger, Z., Shilton, A.K., Luo, C.C., Silverman, E., and Rodal, A.A. (2016). Role of BMP receptor traffic in synaptic growth defects in an ALS model. Mol Biol Cell *27*, 2898–2910.

Dessaud, E., Yang, L.L., Hill, K., Cox, B., Ulloa, F., Ribeiro, A., Mynett, A., Novitch, B.G., and Briscoe, J. (2007). Interpretation of the sonic hedgehog morphogen gradient by a temporal adaptation mechanism. Nature *450*, 717–720.

Digman, M.A., Stakic, M., and Gratton, E. (2013). Raster image correlation spectroscopy and number and brightness analysis. Methods Enzymol *518*, 121–144.

Dowd, C.J., Cooney, C.L., and Nugent, M.A. (1999). Heparan sulfate mediates bFGF transport through basement membrane by diffusion with rapid reversible binding. J. Biol. Chem. *274*, 5236–5244.

Driesch, H. (1891). Entwicklungsmechanische Studien, I. Der Werth der beiden ersten Furchungszellen in der Echinodermenentwicklung. Experimentelle Erzeugen von Theil- und Doppelbildung. Z. Wiss. Zool. *53*, 160–178.

Eldar, A., Dorfman, R., Weiss, D., Ashe, H., Shilo, B.Z., and Barkai, N. (2002). Robustness of the BMP morphogen gradient in *Drosophila* embryonic patterning. Nature *419*, 304–308.

Eldar, A., Rosin, D., Shilo, B.Z., and Barkai, N. (2003). Self-enhanced ligand degradation underlies robustness of morphogen gradients. Dev. Cell *5*, 635–646.

Entchev, E.V., Schwabedissen, A., and González-Gaitán, M. (2000). Gradient formation of the TGF-beta homolog Dpp. Cell *103*, 981–991.

Fried, P., and Iber, D. (2014). Dynamic scaling of morphogen gradients on growing domains. Nat. Commun. *5*, 5077.

Fujise, M., Izumi, S., Selleck, S.B., and Nakato, H. (2001). Regulation of dally, an integral membrane proteoglycan, and its function during adult sensory organ formation of Drosophila. Dev. Biol. *235*, 433–448.

Fujise, M., Takeo, S., Kamimura, K., Matsuo, T., Aigaki, T., Izumi, S., and Nakato, H. (2003). Dally regulates Dpp morphogen gradient formation in the Drosophila wing. Development *130*, 1515–1522.

Gibson, M.C., and Perrimon, N. (2005). Extrusion and death of DPP/BMP-compromised epithelial cells in the developing Drosophila wing. Science *307*, 1785–1789.

Giráldez, A.J., Copley, R.R., and Cohen, S.M. (2002). HSPG modification by the secreted enzyme Notum shapes the Wingless morphogen gradient. Dev. Cell *2*, 667–676.

Gregor, T., Bialek, W., de Ruyter van Steveninck, R.R., Tank, D.W., and Wieschaus, E.F. (2005). Diffusion and scaling during early embryonic pattern formation. Proc. Natl. Acad. Sci. USA *102*, 18403–18407.

Gregor, T., Wieschaus, E.F., McGregor, A.P., Bialek, W., and Tank, D.W. (2007). Stability and nuclear dynamics of the bicoid morphogen gradient. Cell *130*, 141–152.

Hamaratoglu, F., de Lachapelle, A.M., Pyrowolakis, G., Bergmann, S., and Affolter, M. (2011). Dpp signaling activity requires Pentagone to scale with tissue size in the growing Drosophila wing imaginal disc. PLoS Biol. *9*, e1001182.

Harmansa, S., Alborelli, I., Bieli, D., Caussinus, E., and Affolter, M. (2017). A nanobody-based toolset to investigate the role of protein localization and dispersal in Drosophila. eLife *6*, e22549.

Huang, Y., and Umulis, D.M. (2019). Scale invariance of BMP signaling gradients in zebrafish. Sci. Rep. *9*, 5440.

Inomata, H. (2017). Scaling of pattern formations and morphogen gradients. Dev. Growth Differ. *59*, 41–51.

Ishihara, M., Fedarko, N.S., and Conrad, H.E. (1987). Involvement of phosphatidylinositol and insulin in the coordinate regulation of proteoheparan sulfate metabolism and hepatocyte growth. J. Biol. Chem. *262*, 4708–4716.

Ishimatsu, K., Hiscock, T.W., Collins, Z.M., Sari, D.W.K., Lischer, K., Richmond, D.L., Bessho, Y., Matsui, T., and Megason, S.G. (2018). Size-reduced embryos reveal a gradient scaling-based mechanism for zebrafish somite formation. Development *145*.

Jackson, S.M., Nakato, H., Sugiura, M., Jannuzi, A., Oakes, R., Kaluza, V., Golden, C., and Selleck, S.B. (1997). Dally, a Drosophila glypican, controls cellular responses to the TGF-beta-related morphogen, Dpp. Development *124*, 4113–4120.

Kähkönen, T.E., Ivaska, K.K., Jiang, M., Büki, K.G., Väänänen, H.K., and Härkönen, P.L. (2018). Role of fibroblast growth factor receptors (FGFR) and FGFR like-1 (FGFRL1) in mesenchymal stromal cell differentiation to osteoblasts and adipocytes. Mol. Cell. Endocrinol. *461*, 194–204.

Kicheva, A., Pantazis, P., Bollenbach, T., Kalaidzidis, Y., Bittig, T., Jülicher, F., and González-Gaitán, M. (2007). Kinetics of morphogen gradient formation. Science *315*, 521–525.

Kuo, W.J., Digman, M.A., and Lander, A.D. (2010). Heparan sulfate acts as a bone morphogenetic protein coreceptor by facilitating ligand-induced receptor hetero-oligomerization. Mol. Biol. Cell *21*, 4028–4041.

Lander, A.D., Lo, W.C., Nie, Q., and Wan, F.Y. (2009). The measure of success: constraints, objectives, and tradeoffs in morphogen-mediated patterning. Cold Spring Harb. Perspect. Biol. *1*, a002022.

Lander, A.D., Nie, Q., Vargas, B., and Wan, F.Y.M. (2011). Size-normalized robustness of Dpp gradient in Drosophila Wing imaginal disc. J. Mech. Mater. Struct. *6*, 321–350.

Lander, A.D., Nie, Q., and Wan, F.Y. (2002). Do morphogen gradients arise by diffusion? Dev. Cell *2*, 785–796.

Lecuit, T., and Cohen, S.M. (1998). Dpp receptor levels contribute to shaping the Dpp morphogen gradient in the Drosophila wing imaginal disc. Development *125*, 4901–4907.

Lin, X., and Perrimon, N. (1999). Dally cooperates with Drosophila Frizzled 2 to transduce Wingless signalling. Nature *400*, 281–284.

Martín-Castellanos, C., and Edgar, B.A. (2002). A characterization of the effects of Dpp signaling on cell growth and proliferation in the Drosophila wing. Development *129*, 1003–1013.

Nahmad, M., and Stathopoulos, A. (2009). Dynamic interpretation of hedgehog signaling in the Drosophila wing disc. PLoS Biol. *7*, e1000202.

Norman, M., Vuilleumier, R., Springhorn, A., Gawlik, J., and Pyrowolakis, G. (2016). Pentagone internalises glypicans to fine-tune multiple signalling pathways. eLife *5*, e13301.

Ogiso, Y., Tsuneizumi, K., Masuda, N., Sato, M., and Tabata, T. (2011). Robustness of the Dpp morphogen activity gradient depends on negative feedback regulation by the inhibitory Smad. Dad. Dev. Growth Differ. *53*, 668–678.

Oliveira, M.M., Shingleton, A.W., and Mirth, C.K. (2014). Coordination of wing and whole-body development at developmental milestones ensures robustness against environmental and physiological perturbations. PLoS Genet. *10*, e1004408.

Schindelin, J., Arganda-Carreras, I., Frise E, Kaynig V., Longair, M., Pietzsch, T., Preibisch, S., Rueden, C., Saalfeld, S., Schmid, B., et al. (2012). Fiji: an open-source platform for biological-image analysis. Nat. Methods *9*, 676–682.

Setiawan, L., Pan, X., Woods, A.L., O'Connor, M.B., and Hariharan, I.K. (2018). The BMP2/4 ortholog Dpp can function as an inter-organ signal that regulates developmental timing. Life Sci. Alliance *1*, e201800216.

Takeo, S., Akiyama, T., Firkus, C., Aigaki, T., and Nakato, H. (2005). Expression of a secreted form of Dally, a Drosophila glypican, induces overgrowth phenotype by affecting action range of Hedgehog. Dev. Biol. *284*, 204–218.

Tang, B. (1993). Orthogonal array-based Latin hypercubes. J. Am. Stat. Assoc. *88*, 1392–1397.

Tanimoto, H., Itoh, S., ten Dijke, P., and Tabata, T. (2000). Hedgehog creates a gradient of DPP activity in Drosophila wing imaginal discs. Mol. Cell *5*, 59–71.

Teleman, A.A., and Cohen, S.M. (2000). Dpp gradient formation in the Drosophila wing imaginal disc. Cell *103*, 971–980.

Umulis, D.M., and Othmer, H.G. (2013). Mechanisms of scaling in pattern formation. Development *140*, 4830–4843.

Vuilleumier, R., Springhorn, A., Patterson, L., Koidl, S., Hammerschmidt, M., Affolter, M., and Pyrowolakis, G. (2010). Control of Dpp morphogen signalling by a secreted feedback regulator. Nat. Cell Biol. *12*, 611–617.

Wartlick, O., Mumcu, P., Kicheva, A., Bittig, T., Seum, C., Jülicher, F., and González-Gaitán, M. (2011). Dynamics of Dpp signaling and proliferation control. Science *331*, 1154–1159.

Widmann, T.J., and Dahmann, C. (2009). Dpp signaling promotes the cuboidal-to-columnar shape transition of Drosophila wing disc epithelia by regulating Rho1. J. Cell Sci. *122*, 1362–1373.

Wolpert, L. (1969). Positional information and the spatial pattern of cellular differentiation. J. Theor. Biol. *25*, 1–47.

Zhou, S., Lo, W.C., Suhalim, J.L., Digman, M.A., Gratton, E., Nie, Q., and Lander, A.D. (2012). Free extracellular diffusion creates the Dpp morphogen gradient of the Drosophila wing disc. Curr. Biol. *22*, 668–675.

Zinski, J., Bu, Y., Wang, X., Dou, W., Umulis, D., and Mullins, M.C. (2017). Systems biology derived source-sink mechanism of BMP gradient formation. eLife *6*, e22199.

STAR★METHODS

KEY RESOURCES TABLE

REAGENT or RESOURCE	SOURCE	IDENTIFIER
Antibodies		
Rabbit monoclonal anti-Smad3 (phospho S423 + S425), clone EP823Y	Abcam	Cat# ab52903; RRID: AB_882596
Mouse monoclonal anti-*Drosophila* Patched	Developmental Studies Hybridoma Bank	Cat# Drosophila Ptc (Apa 1); RRID: AB_528441
Mouse monoclonal anti-*Drosophila* Wingless protein	Developmental Studies Hybridoma Bank	Cat# 4d4; RRID: AB_528512
Mouse monoclonal anti-*Drosophila* Dally-like protein	Developmental Studies Hybridoma Bank	Cat# Dally-like (13G8); RRID: AB_528191
Mouse monoclonal anti-β-galactosidase	Promega	Cat# Z3781; RRID: AB_430877
Rabbit polyclonal anti-Pentagone	Vuilleumier et al., 2010	N/A
Goat anti-mouse IgG (H+L) cross-adsorbed secondary antibody, Alexa Fluor 488	Thermo Fisher Scientific	Cat# A-11001; RRID: AB_2534069
Goat anti-mouse IgG (H+L) cross-adsorbed secondary antibody, Alexa Fluor 555	Thermo Fisher Scientific	Cat# A-21422; RRID: AB_2535844
Goat anti-rabbit IgG (H+L) cross-adsorbed secondary antibody, Alexa Fluor 647	Thermo Fisher Scientific	Cat# A-21244; RRID: AB_2535812
Chemicals, Peptides, and Recombinant Proteins		
DAPI (4',6-diamidino-2-phenylindole, dihydrochloride)	Thermo Fisher Scientific	Cat# D1306; RRID: AB_2629482
FM4-64FX	Thermo Fisher Scientific	Cat# F34653
Experimental Models: Organisms/Strains		
D. melanogaster: UAS-GFP	Bloomington Stock Center	1521
D. melanogaster: act5C-Gal4	Bloomington Stock Center	3954
D. melanogaster: UAS-pentRNAi (II)	Bloomington Stock Center	51169
D. melanogaster: UAS-pentRNAi (III)	Bloomington Stock Center	41641
D. melanogaster: tubP-Gal80^{ts}	Bloomington Stock Center	7018
D. melanogaster: w^{1118}	Bloomington Stock Center	3605
D. melanogaster: ap-Gal4	Bloomington Stock Center	3041
D. melanogaster: pent^{2}	Vuilleumier et al., 2010	N/A
D. melanogaster: pent-frgII-lacZ	Vuilleumier et al., 2010	N/A
D. melanogaster: UAS-Pent (II)	Vuilleumier et al., 2010	N/A
D. melanogaster: UAS-Pent (III)	Vuilleumier et al., 2010	N/A
D. melanogaster: brk-Gal4	Vuilleumier et al., 2010	N/A
D. melanogaster: pent^{A17}, tkv^{strII}	Gift from G. Pyrowolakis	N/A
D. melanogaster: UAS-GFP-Pent	Gift from G. Pyrowolakis	N/A
D. melanogaster: hh-Gal4	Provided by A. Alnaif	N/A
D. melanogaster: cut-Gal4	Bloomington Stock Center	27327
D. melanogaster: UAS-RFP.W	Bloomington Stock Center	31417
D. melanogaster: hsFLP; act>y>Gal4, UAS-GFP.nls (X;III)	Gift from H. Nakato	N/A
D. melanogaster: dally^{80}	Gift from H. Nakato	N/A
D. melanogaster: UAS-Dally	Gift from H. Nakato	N/A
D. melanogaster: UAS-sflRNAi	Bloomington Stock Center	34601
D. melanogaster: UAS-tkvRNAi	Bloomington Stock Center	40937
D. melanogaster: tkv^{Df}	Gift from T. Tabata	N/A
D. melanogaster: tkv^{Df}, ubi-tkv-HA	Ogiso et al., 2011	N/A

(*Continued on next page*)

Continued

REAGENT or RESOURCE	SOURCE	IDENTIFIER
D. melanogaster: tkv^{a12}, ubi-tkv-HA	Ogiso et al., 2011	N/A
D. melanogaster: ubi-tkv-HA (III)	Ogiso et al., 2011	N/A
D. melanogaster: tkv^{strII}	Bloomington Stock Center	34509
D. melanogaster: en-Gal4	Bloomington Stock Center	30564
D. melanogaster: dpp^{d12}; dpp-Gal4	Zhou et al., 2012	N/A
D. melanogaster: dpp^{d14}; UAS-DppDendra2	Zhou et al., 2012	N/A
D. melanogaster: UAS-tkvmCherry	Deshpande et al., 2016	N/A
D. melanogaster: ds-Gal4	Provided by M. Nahmad	N/A
D. melanogaster: tkv-lacZ	Gift from R. Mann	N/A
Software and Algorithms		
Fiji Is Just ImageJ	Schindelin et al., 2012	fiji.sc
Wolfram Mathematica	Wolfram Research	www.wolfram.com/mathematica/
MATLAB	MathWorks	mathworks.com/products/matlab.htm
Globals for Images · SimFCS	Laboratory for Fluorescence Dynamics at University of California, Irvine	Lfd.uci.edu/globals
Adobe Illustrator	Adobe Inc.	Adobe.com/products/illustrator.html
Microsoft Excel	Microsoft	microsoft.com/en-us/Microsoft-365/excel
Deposited Data		
Mendeley Dataset	Elsevier	https://doi.org/10.17632/37vrnb7yxz.1
Other		
Zeiss LSM 780 laser scanning confocal fluorescence microscope	Zeiss	N/A
Zeiss SteREO Discovery.V8 stereomicroscope	Zeiss	N/A
Olympus FluoView FV1000 confocal microscope	Olympus	N/A

RESOURCE AVAILABILITY

Lead Contact

Further information and requests for resources and reagents should be directed to and will be fulfilled by the Lead Contact, Arthur D. Lander (adlander@uci.edu).

Materials Availability

This study did not generate new unique reagents.

Data and Code Availability

No custom code was used in this study. *Mathematica* and MATLAB packages were used as described below. Original data have been deposited to Mendeley Data: https://doi.org/10.17632/37vrnb7yxz.1

EXPERIMENTAL MODEL AND SUBJECT DETAILS

Drosophila Stocks and Genetics

Species: *Drosophila melanogaster*. Flies were grown in vials filled with medium containing the following ingredients per 1L: 8.4g agar; 63.05g dextrose; 34.225g sucrose; 9.6g potassium sodium tartrate; 0.735g calcium chloride; 76g corn meal; 32g yeast; 4ml propionic acid; 1g tegosept; 10ml 95% ethanol; 0.4ml food coloring. Vials were kept in an incubator with a 12 hour light/dark cycle at 25°C. Crosses were carried out at 25°C except in experiments using the temperature-sensitive Gal80 repressor and heat-shock FLP as follow:

hsFLP; act>y>Gal4>UAS-Pent, UAS-Pent, UAS-GFP: three days at 25°C followed by a 20-minute 37°C heat shock and two more days at 25°C before dissection (Figure 3).

act5C-Gal4, tubPGal80^{ts}>UAS-pentRNAi: 24, 48 or 72 hours at 30°C followed by switch to 18°C until dissection (Figure 7).

act5C-Gal4, tubPGal80^{ts}>UAS-pentRNAi: switch from 18°C to 30°C for 24, 48, 72 or 96 hours before dissection (Figure 7).

Original fly strains used in this article are listed in the Key Resources Table. *Pent^{2},tkv^{Df}, act5C-Gal4,dally^{80}, UAS-Dally,dally^{80}, pent^{2},tkv^{a12},ubi-tkv-HA, pent^{2},dpp^{d12}* and *pent^{2},dpp^{d14}* were generated by standard recombination method. The recombinants were screened by phenotypes of *pent^{2}/pent^{2}, tkv^{Df}/tkv^{strII}, dally^{80}/dally^{80}, act5C-Gal4>UAS-GFP, act5C-Gal4,dally^{80}/UAS-Dally,dally^{80}, tkv^{Df}/tkv^{a12},ubi-tkv-HA* and *dpp^{d12}/dpp^{d14}* (Vuilleumier et al., 2010; Fujise et al., 2003; Ogiso et al., 2011; Zhou et al., 2012) respectively.

Since these larval wing imaginal discs are not sexually dimorphic, both female and male larvae were dissected in 3rd instar stage for imaging of wing discs except for experiments to quantify the effect of co-receptors in the edge (Figure 4) and experiments of scaling quantification (Figures 5 and S3). For those experiments, both female and male larvae were dissected in various stages (from early 2nd instar to late 3rd instar).

Detailed Genotypes

For detailed genotypes used in the study see Table S1.

METHOD DETAILS

Clonal Analysis

The *Act>y>Gal4* transgene was used to generate random GFP marked "flip-out" clones, which were induced by heat-shock of second instar larvae (48-72 hours after egg laying) at 37°C for 20 min, and larvae were allowed to grow at 25°C.

Egg-Laying Assay

Flies were kept in a 25°C incubator and eggs were collected on apple juice agar plates with yeast paste at the center. Prior to egg collection, we treated flies with CO_2 and then let them lay eggs on a plate for 1 h to get rid of old eggs. After that, the flies were transferred to a new plate and the eggs were collected for 1 h. Then collection plates were kept in a 25°C incubator and larvae from these plates were dissected at different hours after egg-laying (AEL).

Conditional Knockdown of *Pent*

Eggs from appropriate crosses were collected as above. These eggs were incubated at 30°C (*pentRNAi* on) for 24 h, 48 h or 72 h after egg laying, before being switched to 18°C, which would turn *pentRNAi* off at approximately early first instar stage, early second instar stage or early third instar stage, respectively. The larvae from these eggs then were dissected at the wandering stage. The larvae from the same crosses were raised at 18°C (*pentRNAi* off) and then switched to 30°C (*pentRNAi* on) for 24 h, 48 h, 72 h or 96 h; at that time only wandering larvae were selected for dissection. This results in *pentRNAi* having been on approximately from early-mid third instar stage, late second-early third instar stage, late first-early second instar stage or first instar stage, respectively.

Antibodies and Immunostaining

For immunostaining, larvae were dissected in ice cold phosphate-buffered saline (PBS) and transferred directly into fix solution (4% paraformaldehyde and 0.05M EGTA in PBS). Samples were fixed for 30 min at room temperature. Samples were then washed extensively 5 times for 10 min each with PBT (0.1% Tween-20 in PBS) and blocked overnight at 4°C in blocking solution (1% BSA, 0.3% Deoxycholate and 0.3% TritonX-100 in PBS). Afterwards, samples were incubated with primary antibodies diluted in blocking solution at 4°C overnight then washed 6 times in PBT for 10 min each, and incubated with secondary antibodies and DAPI diluted in PBT for 1.5 h at room temperature on a rotor. After 5 washes in PBT for 10 min each, stained discs were mounted on slides.

The following primary antibodies were used: rabbit anti-pSmad3 (Abcam, ab52903) 1:1000; mouse anti-Ptc (DSHB, Apa1) 1:1000; mouse anti-Wg (DSHB, 4D4) 1:1000; mouse anti-Dlp (DSHB, 13G8) 1:1000; mouse anti-β-galactosidase (Promega, Z3781) 1:1000; rabbit anti-Pent (Vuilleumier et al., 2010) 1:5000. Alexa Fluor-conjugated anit-rabbit and anti-mouse secondary antibodies were used at 1:1000. 100 μg/mL DAPI were diluted 1:1000 in PBT.

Imaging

Wing discs were dissected from larvae of various stages and mounted in ice cold PBS on slides. The slides were kept on ice for live imaging of *Drosophila* wing discs. Images of both fixed and live wing discs were obtained with a Zeiss LSM 780 laser scanning confocal fluorescence microscope.

For imaging of *Drosophila* adult wings, flies were preserved in 70% ethanol. After the 70% ethanol was removed, the wings were plucked and mounted in 50% Canada balsam in xylene on slides. Images of wings were obtained with a Zeiss SteREO Discovery.V8 stereomicroscope.

Images were analyzed using Fiji and processed using Adobe Illustrator.

Fluorescence Correlation Spectroscopy (FCS) and Cross-correlation Raster Image Correlation Spectroscopy (ccRICS)

Single point FCS (Zhou et al., 2012) and ccRICS (Digman et al., 2013) were performed using an Olympus FluoView FV1000 confocal microscope with a 60x/1.2 water immersion objective. Data were analyzed with SimFCS software (Laboratory for Fluorescence

Dynamics, University of California, Irvine). Each FCS measurement lasted for 100 seconds. To collect ccRICS data, the following settings were applied: pixel size 0.077 μm, pixel dwell time 10 μs, line time 3.83 ms, region size 96 pixels X 96 pixels. Then data were analyzed with SimFCS software. Images were processed using Adobe Illustrator.

Mathematical Modeling

The system of partial differential equations used to model the Dpp gradient on a growing wing disc is shown below as Equation 1, and also diagrammed as a conceptual network (Figure S8). The modeled domain consists of the intercellular (basolateral) spaces of the posterior compartment of the wing disc, which is represented as a one-dimensional reaction-diffusion system. The one-dimensional approximation assumes that morphogen flux in the dorsoventral and apicobasal directions is negligible. This is probably a good assumption at large disc sizes, but, as described later (see "influence of dimensionality on source-sink scaling"), and in Lander et al., 2011, may be less so at small size. We model the basal rates of synthesis of gene products as constant in time and space, as modified by pMad or Brk, except in the following cases: we lower Tkv production and raise coreceptor production in the Dpp-production region, to capture known effects of Hedgehog signaling in that region (Tanimoto et al., 2000). In addition, we model the basal rate of Brk synthesis as continuously increasing during disc growth, in order to fit the data of (Hamaratoglu et al., 2011), who show that peak Brk levels rise more than 10-fold over the course of wing disc development (because peak Brk expression occurs where Dpp signaling is essentially negligible, such changes cannot be attributed to an effect of Dpp). We model growth of wildtype discs to fit our own observations of disc growth rate (Figure S3), which are similar to those published by (Wartlick et al., 2011). For some genotypes, including homozygous *pent* mutants, we adjusted the growth rate (described further below) so that discs finish growing at a smaller size, in accordance with published data on *pent* discs (Ben-Zvi et al., 2011a; Vuilleumier et al., 2010), and our own observations (Figures 5 and S6).

$$\frac{\partial[Dpp]}{\partial t}+\frac{\partial(V[Dpp])}{\partial x}=\frac{v_{dpp}}{1+\left(\frac{x}{prod(t)}\right)^{20}}+D_{dpp}\Delta[Dpp]-k_1[Dpp][Tkv]+k_{r1}[Dpp-Tkv]-k_2[Dpp][Cr]+k_{r2}[Dpp-Cr]$$

$$-\frac{d_{dpp}}{1+\left(\frac{x}{prod(t)}\right)^{20}}[Dpp],$$

$$\frac{\partial[Tkv]}{\partial t}+\frac{\partial(V[Tkv])}{\partial x}=v_{tkv}-k_1[Dpp][Tkv]+k_{r1}[Dpp-Tkv]-k_4[Tkv][Dpp-Cr]+d_{dpptkv}[Dpp-Tkv]+d_{dpptkv*}[Dpp-Tkv*]$$

$$-d_{tkv}[Tkv],$$

$$\frac{\partial[Cr]}{\partial t}+\frac{\partial(V[Cr])}{\partial x}=v_{cr}-k_2Dpp]Cr]+k_{r2}Dpp-Cr]+k_4Tkv]Dpp-Cr]-k_3[Pent]_{in}[Cr]-d_{cr}[Cr],$$

$$\frac{\partial[Dpp-Tkv]}{\partial t}+\frac{\partial(V[Dpp-Tkv])}{\partial x}=k_1[Dpp][Tkv]-k_{r1}[Dpp-Tkv]-k_5[Cr][Dpp-Tkv]-d_{dpptkv}[Dpp-Tkv],$$

$$\frac{\partial[Dpp-Tkv*]}{\partial t}+\frac{\partial(V[Dpp-Tkv*])}{\partial x}=k_5[Cr][Dpp-Tkv]+k_4[Tkv][Dpp-Cr]-d_{dpptkv*}[Dpp-Tkv^*],$$

$$\frac{\partial[Dpp-Cr]}{\partial t}+\frac{\partial(V[Dpp-Cr])}{\partial x}=k_2[Dpp][Cr]-k_{r2}[Dpp-Cr]-k_4[Tkv][Dpp-Cr]-d_{dppcr}[Dpp-Cr],$$

$$\frac{\partial[pMad]}{\partial t}+\frac{\partial(V[pMad])}{\partial x}=v_{pmad}[Dpp-Tkv*]-d_{pmad}[pMad],$$

$$\frac{\partial[brk]}{\partial t}+\frac{\partial(V[brk])}{\partial x}=\frac{x_{\max}v_{brk}}{\left(1+\left(\frac{[pMad]}{EC_{brk}}\right)^2\right)}-d_{brk}[brk],$$

$$\frac{\partial[TF]}{\partial t}+\frac{\partial(V[TF])}{\partial x}=\frac{v_{tf}}{1+\left(\frac{[brk]}{EC_{TF}}\right)^2}-d_{tf}[TF],$$

$$\frac{\partial[Pent]_{out}}{\partial t}+\frac{\partial(V[Pent]_{out})}{\partial x}=\frac{v_{pent}}{1+\left(\frac{[pMad]}{EC_{pent}}\right)^2}+D_{pent}\Delta[Pent]_{out}-k_6[Pent]_{out},$$

$$\frac{\partial[Pent]_{in}}{\partial t}+\frac{\partial(V[Pent]_{in})}{\partial x}=k_6[Pent]_{out}-d_{pent}[Pent]_{in}.$$

$$v_{tkv}=tkv1+\frac{tkv2}{1+\left(\frac{[TF]}{EC_{tkv}}\right)^2}+\frac{tkv3}{1+\left(\frac{x}{prod(t)}\right)^{-20}},\ v_{cr}=cr1+\frac{cr2}{1+\left(\frac{[TF]}{EC_{Cr}}\right)^2}+\frac{cr3}{1+\left(\frac{x}{prod(t)}\right)^{20}}. \quad \text{(Equation 1)}$$

In the above system of equations, $[P](x,t)$ denotes the concentration of species P at location x and at time t. To represent the likely fact that Pent must first bind cells to have effects on HSPGs, Pent has unbound and bound forms in the model, represented by $[Pent]_{out}$ and $[Pent]_{in}$, respectively. The spatial domain $[0, x_{max}(t)]$ represents the region of the posterior compartment. To represent disc growth, x_{max} increases according to: $x_{max}(t)=x_0 e^{at_2F_1\left(1,\frac{1}{n},1+\frac{1}{n},-bt^n\right)}$ (derivation below). Dpp and unbound Pent ($[Pent]_{out}$) are the only diffusive species in this model, and have diffusion coefficients D_{dpp} and D_{pent}, respectively. The term $\frac{\partial(V[P])}{\partial x}$ can be split into two terms $[P]\frac{\partial V}{\partial x}$ and $V\frac{\partial[P]}{\partial x}$ representing dilution and advection driven by disc growth, respectively. $V(x,t)$ is the disc growth velocity at location x and its value at x_{max} represents the growth rate of the entire posterior compartment: $V(x_{max},t)=\frac{dx_{max}}{dt}$. We assume the disc grows homogeneously over the entire space, and $V(x,t)$ is a linear function of x:

$$V(x,t)=\frac{x}{x_{max}(t)}V(x_{max},t). \quad \text{(Equation 2)}$$

For any species P and Q, $k_i[P][Q]$, $(i=1,2,3,4,5)$, are association rates between P and Q, and $k_{ri}[PQ]$ $(i=1,2)$ are dissociation rates of the complex PQ formed by P and Q. For any species P, $d_P[P]$ represents a degradation rate for (free) P.

The rate constant k_6 describes first order association of $Pent_{out}$ with cells to produce the bound species $Pent_{in}$. We assume that Dpp is synthesized in a localized source (termed the production region), and the size of Dpp production region grows at the same rate as the rest of posterior compartment. Specifically, we take $prod(t)=p*x_{max}(t)$, with p=0.12. Dpp production is then modeled by $v_{dpp}/(1+(x/prod(t))^{20})$. The high-exponent Hill function essentially approximates a step function. A Dpp degradation term is also added in the production region: $d_{dpp}/(1+(x/prod(t))^{20})$.

The production rate of Tkv, v_{tkv}, contains three terms: *tkv1* is a base production rate in the entire disc; $tkv2/(1+([TF]/EC_{tkv})^2)$ represents the production regulated by TF, which stands for downstream transcription factors repressed by Brinker (Brk); Tkv synthesis is low inside the Dpp production region due to the effect of Hedgehog (Tanimoto et al., 2000) and $tkv3/(1+(x/prod(t))^{-20})$ is used to model the additional Tkv production outside of the production region. Dally and Dlp are lumped together as "Co-receptor" (Cr) in this model. The production rate of co-receptor, v_{cr}, contains three terms: *cr1* is base production rate; $cr2/(1+([TF]/EC_{Cr})^2)$ represents the production regulated by TF; and because co-receptor synthesis is high inside Dpp production region, due to effect of Hedgehog (Tanimoto et al., 2000), $cr3/(1+(x/prod(t))^{20})$ is used to model the addition Cr production in the Dpp production region. To represent the fact that $Pent_{in}$ drives destruction of co-receptors, we introduce a decay term into the equation for Cr that is proportional to the level of $Pent_{in}$ with proportionality constant k_3.

To model the production of Brinker (Brk), which is repressed by pMad, we multiply a basal production rate by $1/(1+[pMad]/EC_{brk})^2)$, however, because basal Brk production appears to increase markedly with disc size (Hamaratoglu et al., 2011), we take the basal production rate to be a constant v_{brk} times x_{max} (disc diameter). To model the production of TF, we multiply a basal production rate v_{tf} by $1/(1+[Brk]/EC_{TF})^2)$. To model the production of Pent, we multiply a basal production rate v_{Pent} by $1/(1+[pMad]/EC_{Pent})^2)$.

The biochemical steps in the assembly of the active form of the Dpp receptor are modeled to reflect that fact that TGF-beta family receptors assemble in a two-stage process which, for the BMP branch of the TGF-beta family, usually involves initial binding to type I receptors (e.g. Tkv) and subsequent recruitment of type II receptors. Thus, the species DppTkv may be construed to represent complexes that lack type II receptors while the species DppTkv* represents complexes containing both type I and II receptors.

We model co-receptor activity according to the results of (Kuo et al., 2010), who showed that HSPGs catalyze the conversion of BMP-type I receptor complexes into BMP-type I receptor-type II receptor complexes. Rate constant k_5 captures this behavior. At the same time, because Dpp can bind HSPGs, we also model direct reversible binding, and allow for the possibility that Dpp initially bound to HSPGs can also recruit type I and type II receptors; this latter behavior is captured by k_4, but as described later, the value of k_4 may be set effectively to zero without having significant effect on the model output.

In solving system (1) over time and space it is necessary to specify initial conditions for all variables and boundary conditions for the diffusing species Dpp and Pent. The boundary conditions are no-flux at $x=0$, i.e. $\left.\frac{d[P]}{dx}\right|_{x=0} = 0$, and absorbing at x_{max}, i.e. $[P]|_{x=x_{max}(t)} = 0$, where P stands for either Dpp or Pent. The no-flux condition is justified by the symmetry of the problem (anterior and posterior compartments are taken to be symmetric about the A-P boundary), and the absorbing condition creates a generalized sink at $x=x_{max}$.

The initial posterior compartment size is taken to be 0.1 μm—smaller than the actual size of discs—in order to provide sufficient simulation time for results to become independent of initial conditions. The initial conditions are then obtained by running the simulation in the fixed initial domain for 4 hours starting from zero values for all species. We verified that these conditions produced results that were independent of initial condition choices.

The total simulation time is 120 hours. We take time=0 to correspond to 24 hours after egg laying, which is consistent with the convention adopted by (Wartlick et al., 2011). Because the rate at which discs grow is not constant, but slows as larval development proceeds, it was necessary to use an empirically determined growth rate function in the model. To obtain this, we measured compartment sizes experimentally (Figure S3). To fit those data to a simple equation we considered the following function which describes an arbitrary system that is growing exponentially but slowing according to a declining Hill function of time.

$$\begin{cases} \frac{dx_{max}}{dt} = \frac{ax_{max}}{1+bt^n} = f(x_{max}, t) \\ x_{max}(0) = x_0. \end{cases} \quad \text{(Equation 3)}$$

The general solution to (3) is $x_{max}(t) = x_0 e^{at\,{}_2F_1\left(1,\frac{1}{n},1+\frac{1}{n},-bt^n\right)}$, where ${}_2F_1$ is the hypergeometric function:

$${}_2F_1(a,b;c;z) = \sum_{n=0}^{\infty} \frac{(a)_n (b)_n}{(c)_n} \frac{z^n}{n!}. \quad \text{(Equation 4)}$$

Here $(q)_n$ is the Pochhammer symbol, defined by:

$$(q)_n = \begin{cases} 1, & n=0; \\ q(q+1)\cdots(q+n-1), & n>0. \end{cases} \quad \text{(Equation 5)}$$

We used the built-in function *NonlinearModelFit* in Mathematica to fit the experimental data (Figure S3) to the above function. By testing various integers n, the best fit was found to be given by n=3. We then used this function to describe the growth of x_{max} over time in the model. Although the mathematical form is different from that proposed by (Wartlick et al., 2011) for the wing disc, the two functions are very similar in shape.

Lagrangian Framework for Solving Mathematical Equations

The spatial domain of Equation 1 is time-dependent, whereas PDEs solvers usually require a fixed domain. We therefore use the following linear coordinate transformation to transfer the dynamical spatial domain onto a fixed domain:

$$\begin{cases} x = r(\tau)X \\ t = \tau \end{cases}. \quad \text{(Equation 6)}$$

where $r(\tau) = \frac{x_{max}(\tau)}{x_0}$. The transferred spatial domain is $X \in [0, x_0]$, where x_0 is the initial posterior compartment size shown in Equation 3. Derivatives in the Lagrangian coordinate system (X, τ) have the following relationships to derivatives in the original coordinate system (x, t):

$$\begin{cases} \frac{\partial}{\partial X} = r\frac{\partial}{\partial x} \\ \frac{\partial^2}{\partial X^2} = r^2\frac{\partial^2}{\partial x^2} \\ \frac{\partial}{\partial \tau} = \frac{\partial}{\partial t} + \frac{\partial}{\partial x}\frac{\partial x}{\partial \tau} = \frac{\partial}{\partial t} + \frac{1}{r}\frac{dr}{d\tau}\frac{\partial}{\partial X} \end{cases} \quad \text{(Equation 7)}$$

The transformed growth velocity $\tilde{V}(X, \tau)$ has a similar relationship to Equation 2

$$\tilde{V}(X, \tau) = \frac{X}{x_0}\tilde{V}(x_0, \tau). \quad \text{(Equation 8)}$$

Using Equations 7 and 8, we have

$$\frac{\partial V}{\partial x} = \frac{1}{r}\frac{\partial \tilde{V}}{\partial X} = \frac{1}{r}\frac{1}{x_0}\tilde{V}(x_0, \tau) = \frac{f(x_{max}(\tau), \tau)}{x_{max}(\tau)}. \quad \text{(Equation 9)}$$

For any equation in Equation 1 with the general form

$$\frac{\partial[P]}{\partial t}+\frac{\partial(V[P])}{\partial x}=F([P],x,t)+D\Delta[P]. \quad \text{(Equation 10)}$$

the transformed equation in Lagrangian coordinate is given by

$$\frac{\partial[P]}{\partial \tau}=D\left(\frac{x_0}{x_{\max}}\right)^2\frac{\partial^2[P]}{\partial X^2}+F([P],r(\tau)X,\tau)-\frac{f(x_{\max}(\tau),\tau)}{x_{\max}(\tau)}[P]. \quad \text{(Equation 11)}$$

Since both boundary conditions are homogeneous, the transformed equation inherits the boundary conditions from the original condition: absorbing boundary at one side and no-flux boundary at the other. We solved the transformed equations using PDEs solver *pdepe* in MATLAB 2015b.

Parameter Selection

There are 36 potentially free parameters in the set of Equation 1. We fixed D_{dpp} and k_1 to match values in the literature (see Table S2). In the absence of direct measurements of Pent diffusivity, we set the value of D_{pent} to be the same as D_{dpp}, i.e. 20 μm^2 sec^{-1}. To match the observed apparent decay length of Pent (~8 μm), we fixed k_6 at 0.313 sec^{-1}. The remaining 32 parameters were logarithmically sampled across intervals of several orders of magnitude. Deeply sampling a 32-dimensional space at random is, of course, prohibitive (covering as few as three points in each dimension requires $>10^{15}$ parameter sets), so an iterative procedure was used to converge on reasonable parameter values.

To begin with, parameter selection was subjected to certain constraints even prior to generating numerical solutions. These constraints reflected the requirement that values of λ_{app} for Dpp, when measured outside of the Dpp production region, should be no higher than about 30 μm for Dpp. In general, when field size $>>\lambda_{app}$ so that boundaries play a minimal role in determining gradient shapes (e.g. toward the end of disc growth), we expect $\lambda_{app} \sim \lambda_{intrinsic}$, where

$$\lambda_{intrinsic}=\sqrt{\frac{D}{k_{rem}}} \quad \text{(Equation 12)}$$

Here D is the diffusion coefficient and k_{rem} is an effective removal rate constant. For any diffusing species, an explicit expression for k_{rem}, as a function of x and t, can be found by taking the right-hand side of the equation for that species, dropping diffusion and production terms, multiplying by –1, and dividing the remaining terms by the concentration of that species. For example, for Dpp,

$$k_{rem,Dpp}(x,t)=k_1[Tkv]+k_2[Cr]-\frac{k_{r1}[DppTkv]-k_{r2}[DppCr]}{[Dpp]} \quad \text{(Equation 13)}$$

the last term of which may be neglected at locations far from the Dpp source. In contrast, for $Pent_{out}$,

$$k_{rem,Pent}(x,t)=k_6 \quad \text{(Equation 14)}$$

As placing a ceiling on $\lambda_{intrinsic}$ equates to placing a floor on k_{rem}, the required constraints on $\lambda_{intrinsic}$ for Pent and Dpp constrain $k_1[Tkv]+k_2[Cr]$ and k_6 respectively. As [*Tkv*] and [*Cr*] have maximum possible values of $tkv1/d_{tkv}$ and $cr1/d_{cr}$, the constraint that $\lambda_{intrinsic,Dpp} \leq 30$, implies $k_1 tkv1/d_{tkv} + k_2 cr1/d_{cr} \geq D_{dpp}/900$.

To find parameter sets that fit experimental data, Latin Hypercube sampling (Tang, 1993) was used as a high dimensional random number generator, and Equation 1 solved as described above. Using a multi-step procedure (described below), we selected parameter sets based on their ability to fit dynamic data for eight genotypes: wildtype; $pent^{+/-}$; $pent^{-/-}$; ubi-*tkv*; uniform *dally*; ubi-*tkv*, uniform *dally*; ubi-*tkv*, $pent^{-/-}$; ubi-*tkv*, uniform *dally*, $pent^{-/-}$. Numerical solutions for each of these conditions were obtained by altering appropriate parameters from their wildtype values. For ubi-*tkv* (Tkv uniformly expressed in the entire disc), we took *tkv2*=*tkv3*=0, and *tkv1* to be an adjustable parameter. Similarly, for uniform *dally*, we took *cr2*=*cr3*=0, and *cr1* to be an adjustable parameter. For $pent^{+/-}$, we lowered the production rate of *pent* by half. To model double and triple mutants, we combined several of these alterations.

STEP 1: First, we randomly sampled all parameters in a wide range to find sets that produced roughly good decay lengths for wildtype and $pent^{-/-}$ conditions. The "k^*" parameters (k_1, k_2, k_3, k_4, k_5, k_{r1}, k_{r2}) were sampled over seven orders of magnitude (10^{-8},10^{-1}). Production rates (e.g. *tkv1*, *cr1*, v_{pent}) were sampled over two orders of magnitude (10^{-5},10^{-3}). Degradation rates (e.g. d_{dpp}, d_{tkv}) were sampled over two orders of magnitudes (10^{-6},10^{-4}). EC50s (e.g. EC_{pent}) were sampled over two orders of magnitude (10^{-3},10^{-1}). 500,000 independent parameter sets were explored. Parameters were selected based on their ability to meet constraints on $\lambda_{intrinsic}$ (as discussed above), plus the following constraints on the observed λ_{app} for pMad (where λ_{app} was determined by identifying the location where pMad declines to 1/*e* of its maximum value outside of the production region):

$$\text{For wildtype}: \begin{array}{l} 1.\ \max\limits_{s\in(0,s_{\max})}\ \lambda_{app}\in[12,20] \\ 2.\ \max\limits_{s\in(0,s_{\max})}\ \lambda_{app}-\lambda_{app}(s_{\max})\leq 5 \end{array}$$

$$\text{For pent} - \Big/ - : \begin{array}{l} 1.\ \max\limits_{s\in(0,s_{\max})} \lambda_{app} \le 12 \\ 2.\ \max\limits_{s\in(0,s_{\max})} \lambda_{app} - \lambda_{app}(s_{\max}) \ge 5 \end{array}$$

Here $\lambda_{app}(s)$ is understood as the apparent decay length of pMad when the size of posterior compartment is s μm. The maximum value of s is 196 μm.

STEP 2: Starting from one selected parameter set from STEP1, we randomly perturbed 11 parameters– k_1, k_2, k_3, k_4, k_5, k_{r1}, k_{r2}, EC_{tf}, EC_{brk}, EC_{tkv} and EC_{pent}. The "k" parameters were varied over two orders of magnitude, and the "EC" parameters varied between 0.25 and 4-fold (as before, random numbers were sampled logarithmically). 100,000 independent parameter sets were explored. Parameters were first tested for their ability to meet constraints on $\lambda_{\text{intrinsic}}$ (as discussed above), and results then tested for the ability to meet the following constraints on λ_{app} for pMad:

$$\text{For wildtype} : \begin{array}{l} 1.\ \max\limits_{s\in(0,s_{\max})} \lambda_{app} \in [14, 17] \\ 2.\ \max\limits_{s\in(0,s_{\max})} \lambda_{app} - \lambda_{app}(s_{\max}) \le 2 \end{array}$$

$$\text{For pent} - \Big/ - : \begin{array}{l} 1.\ \max\limits_{s\in(0,s_{\max})} \lambda_{app} \in [3.5, 7] \\ 2.\ \max\limits_{s\in(0,s_{\max})} \lambda_{app} - \lambda_{app}(s_{\max}) \le 2 \end{array}$$

STEP 3: From 18 parameter sets passing the above tests, four were selected for further exploration. we perturbed all parameters over a range from 0.5-2-fold, keeping those that met the following constraints. 500,000 perturbations were carried out for each initial parameter set.

$$\text{For wildtype} : \begin{array}{l} 1.\ \max\limits_{s\in(0,s_{\max})} \lambda_{app} \in [14.5, 16.5] \\ 2.\ \max\limits_{s\in(0,s_{\max})} \lambda_{app} - \lambda_{app}(s_{\max}) \le 2 \end{array}$$

$$\text{For pent} - \Big/ - : \begin{array}{l} 1.\ \max\limits_{s\in(0,s_{\max})} \lambda_{app} \in [4.5, 6.5] \\ 2.\ \max\limits_{s\in(0,s_{\max})} \lambda_{app} - \lambda_{app}(s_{\max}) \le 2 \end{array}$$

$$\text{For ubi} - \text{tkv} : \begin{array}{l} 1.\ \max\limits_{s\in(0,s_{\max})} \lambda_{app} \le 17 \\ 2.\ \max\limits_{s\in(0,s_{\max})} \lambda_{app} - \lambda_{app}(s_{\max}) \le 1 \end{array}$$

$$\text{For uniform dally} : \begin{array}{l} 1.\ \max\limits_{s\in(0,s_{\max})} \lambda_{app} \le 17 \\ 2.\ \max\limits_{s\in(0,s_{\max})} \lambda_{app} - \lambda_{app}(s_{\max}) \le 1 \end{array}$$

For ubi-*tkv*; uniform *dally*: $\max\limits_{s\in(0,s_{\max})} \lambda_{app} \in [5, 8]$

Nine parameter sets passed all of the tests, and one was selected for further refinement. We examined the dynamic behavior of selected parameter sets to identify ones that fit observations reasonably well. We carefully inspected levels and distributions of all species, manually adjustng some parameters to better match prior knowledge: e.g. scaling of λ_{app} for total Dpp; Dpp and pMad gradient shapes that are close to exponential at the end of larval development; degrees of central-suppression of Tkv and Cr at the end of larval development that are consistent with observations; spatial patterns for Tkv, Cr, Brk and Pent that are consistent with observations; and levels of total Dpp inside cells that are much higher than outside (Kicheva et al., 2007; Zhou et al., 2012).

The final parameter set that was selected is given in Tables S2 and S3. Also shown are the parameters *a*, *b* and *n* that appear in growth rate Equation 3. As shown in Figure S3, homozygous *pent* mutant discs grow more slowly than wild type discs, and therefore are fit with a different value of parameter *b*. Although we did not produce full growth curves for all genotypes, the distribution of posterior compartment sizes that we observed suggests that all of the genotypes that scale poorly (ubi-*tkv*, $pent^{-/-}$; uniform *dally*, $pent^{-/-}$; ubi-*tkv*, uniform *dally*; ubi-*tkv*, uniform *dally*, $pent^{-/-}$) grow at a rate similar to $pent^{-/-}$, whereas the others grow at a rate similar to wild-type (i.e. $pent^{+/-}$; ubi-*tkv*; uniform *dally*). The value of *b* used in simulation was therefore selected accordingly from the wildtype and the $pent^{-/-}$ values. The results of the numerical solutions for each genotype are shown in Figure S9.

Simulating Rescue by Compartment-wide Pent Overexpression; Evaluating the Necessity for Pent Diffusivity

The *pent* phenotype in adult wings can be rescued by overexpressing Pent uniformly throughout the wing disc (Vuilleumier et al., 2010) or throughout the posterior compartment (Figure S1). To see whether the model and the parameters that were selected reproduce this behavior, we modified Equation 1 to replace the equation for $[Pent]_{out}$ with

$$\frac{\partial [Pent]_{out}}{\partial t} + \frac{\partial (V[Pent]_{out})}{\partial x} = v_{pent} + D_{pent} \Delta [Pent]_{out} - k_6 [Pent]_{out},$$

Here v_{pent} is a uniform source term that was set to 1.71×10^{-10} M sec^{-1}. The results of numerical simulation are shown in (Figure S9I). They show that, in the model, by the end of disc growth, posterior compartment-wide overexpression of Pent almost fully rescues the Pent phenotype.

Some of the experiments in the manuscript raise the question of whether Pent needs to diffuse at all to carry out its functions. To explore this question, we re-ran the results of the wildtype case using a value of D_{pent} of 0.01 μm^2 sec^{-1}, a factor of 2000 times smaller than had been used before. This change lowers $\lambda_{intrinsic}$ for Pent from 8 μm to 0.18 μm, i.e. it makes Pent effectively indiffusible. We compare the effect of this change on the time course of pMad apparent decay lengths in all of the above mutant scenarios. As can be seen, there is very little difference in the outcomes of these simulations whether Pent diffuses rapidly, or hardly at all (Figure S10A).

To determine whether the qualitative behaviors of the system are strongly dependent on the choice of parameters values, we systematically varied all parameters up and down 10-fold, and measured the effect on λ_{app} of pMad. Specifically, we calculated the ratio between λ_{app} at the end of the simulation for the unperturbed case and the perturbed case. This was done for four genotypes (wildtype; $pent^{-/-}$; ubi-*tkv*; uniform *dally*) (Table S4). Most perturbations produced relatively small changes. Specifically, the system is relatively insensitive to D_{pent}, k_4, k_5, k_6, k_{r1}, k_{r3}, *tkv3*, *cr3*, d_{dpp} and d_{dpptkv}, whereas it is relatively sensitive to D_{dpp}, k_1, k_2, k_3, v_{pent}, d_{pmad}, d_{pent}, v_{dpp} and EC_{pent}. Sensitivity to D_{dpp} is to be expected, of course, because at the end of the simulation, λ_{app} for pMad mirrors $\lambda_{intrinsic}$ for Dpp which, by definition varies with the square root of D_{dpp}. By the same token, almost any change in D_{dpp} can be compensated for by a commensurate change in association rate constants k_1 or k_2 that preserves $\lambda_{intrinsic}$ for Dpp. In other words, even though parameters were selected using a model in which the value of D_{dpp} was fixed, the ability of the model to fit the data does not place constraints on the choice of D_{dpp}.

A Reduced Model that Exhibits Pseudo-Source-Sink Behavior

We may illustrate the principle of pseudo-source-sink scaling using a much simpler model than (1). In this model, shown below, only three species are considered: ligand ([L]), receptor ([R]) and the complex between ligand and receptor ([LR]).

$$\begin{cases} \dfrac{d[L]}{dt} = D\Delta\left[L\right] + \{v_L - d_L[L], \text{ if } x<0.12x_{max} - k_{on}[L][R], \text{ if } x \geq 0.12x_{max} \\ \dfrac{d[R]}{dt} = \dfrac{v_R}{1+(g[LR])^2} - k_{on}[L][R] - d_R[R], \\ \dfrac{d[LR]}{dt} = k_{on}[L][R] - d_{LR}[LR]. \end{cases} \quad \text{(Equation 15)}$$

The spatial domain is $[0,x_{max}]$. The effects of dilution and advection are neglected, as their impact on the full model turned out to be minimal (at least for the parameters chosen in Figures 5J and 6). This enabled us to solve the system at steady state on a variety of fixed domain sizes, rather than model continuous domain growth. As in the full model, ligand is produced in a localized production region that grows proportionately with the rest of the disc. The morphogen diffuses and binds receptors, but here, dissociation from receptors is neglected as it is thought to be slow; the binding event may be understood as representing the combination of binding, uptake and destruction in a single step. Inside the morphogen production region, where we know that receptor and co-receptor levels are handled differently than elsewhere, we replace the usual receptor interaction term with a first order morphogen decay term $d_L[L]$, meant to represent the aggregate of those interactions within the production region. The production of receptor is subject to negative feedback from the amount of complex [*LR*] (which is taken to be a proxy for "signal" from the morphogen). Parameter g is the reciprocal of an EC_{50}, and it reflects the strength of feedback. Setting g=0 is equivalent to removing feedback.

We can non-dimensionalize this system to make both time and space unitless. The three species in (15) are thus re-named according to:

$$\begin{cases} \mu = \dfrac{k_{on}}{d_R}[L], \\ \rho = \dfrac{d_R}{v_R}[R], \\ \omega = \dfrac{d_R}{v_R}[LR]. \end{cases} \quad \text{(Equation 16)}$$

For receptor [R] and the complex [LR], this transformation is equivalent to normalization to the level of free receptor that would obtain in the absence of any feedback or ligand, $R_{max} = \frac{v_R}{d_R}$. We also nondimensionalize space by defining the unit of distance to be λ_0, the intrinsic decay length that would be observed in the absence of ligand binding or feedback:

$$\lambda_0 = \sqrt{\frac{D}{k_{on}R_{max}}} = \sqrt{\frac{Dd_R}{k_{on}v_R}}. \quad \text{(Equation 17)}$$

Finally, we may nondimensionalize time by scaling it to the inverse of the degradation rate of receptor d_R (although the time scale is not relevant to the steady state analysis of (15) it simplifies numerical solution by time-evolution). Thus, the transformation from original coordinates (x,t) to the new coordinates (X,τ) is given by:

$$\begin{cases} X = \frac{x}{\lambda_0}, \\ \tau = td_R. \end{cases} \quad \text{(Equation 18)}$$

The nondimensionalized equations are therefore given by

$$\begin{cases} \frac{d\mu(X,\tau)}{d\tau} = k\Delta\mu(X,\tau) + \begin{cases} -k\phi\mu(X,\tau) + k\upsilon, & \text{if } X<0.12X_{max} \\ -k\mu(X,\tau)\rho(X,\tau), & \text{if } X\geq 0.12X_{max} \end{cases}, \\ \frac{d\rho(X,\tau)}{d\tau} = \frac{1}{1+(\gamma\omega(X,\tau))^2} - \mu(X,\tau)\rho(X,\tau) - \rho(X,\tau), \\ \frac{d\omega(X,\tau)}{d\tau} = \mu(X,\tau)\rho(X,\tau) - \xi\omega(X,\tau). \end{cases} \quad \text{(Equation 19)}$$

The five nondimensional free parameters in (Equation 19) are related to the parameters in (Equation 15) according to:

$$\begin{cases} k = \frac{k_{on}v_R}{d_R^2}, \\ \phi = \frac{d_L d_R}{k_{on}v_R} \\ \upsilon = \frac{v_L}{v_R}, \\ \xi = \frac{d_{LR}}{d_R}, \\ \gamma = g\frac{v_R}{d_R}. \end{cases} \quad \text{(Equation 20)}$$

In addition, X_{max}, the spatial size of the domain scaled to λ_0, enters as a sixth parameter that is required to specify the boundary condition opposite the production region. At the start of the production region we impose a no-flux boundary condition, to reflect the spatial symmetry of the system. At the end of the gradient region, $x=x_{max}$, we impose an absorbing boundary condition.

The steady-state shapes of a series of eight gradients associated with increasing compartment sizes are shown in Figure S10B. Curves are color-coded to represent increasing domain sizes (which, in this case were X_{max} = 1, 2, 3, 4, 5, 6, 9, and 12. To obtain the results labeled "No Feedback", we set the feedback strength γ to zero, and adjusted the morphogen production rate to match so that the results for LR near the origin would be similar in the two cases. The third panel of each of these cases is reproduced in Figures 6C and 6D, and shows how feedback enables gradients to remain quasi-linear, and continue scaling, for much longer. Note also the growing suppression of receptor expression in the Feedback case.

To more thoroughly understand the behavior of the reduced model, we explored a large number of random parameters. It is clear, from (Equation 19) that the parameter k drops out in the steady state, so that in any exploration of parameters in which we are only interested in steady-state behavior we can simply fix k to be 1. We then randomly generated ϕ, ν, ξ and X_{max} using Latin hypercube sampling, initially running simulations with no feedback (γ=0). A total simulation time of T=10,000 allowed us to obtain a steady-state solution numerically. The numerical steady-state solution of ligand-receptor complex is denoted by $\omega(X)_{SS}^{noFB}$. Next, we ran simulations with feedback. Rather than choose values of γ at random, we selected them so as to exclude those that would provide only trivial amounts of feedback, as well as those that would provide so much feedback that receptors would be fully suppressed from the start. In particular, we chose γ as defined by

$$\gamma = \frac{1}{0.25\max\limits_{X\in[0,X_{max}]}\omega(X)_{SS}^{noFB}}. \quad \text{(Equation 21)}$$

We compare the results of feedback and no-feedback scenarios for 1000 randomly generated parameter sets in Figure S10C. They are plotted as in Figure 6E, with the apparent decay length λ_{app} (normalized to λ_0, where λ_0 is effectively equivalent to $\lambda_{intrinsic}$ in the absence of feedback; note the logarithmic axis) being plotted against the field size (normalized to λ_0).

Note the ability of feedback to produce values of λ_{app} much greater than observed without feedback. This effect is even more apparent if we eliminate those cases in which receptor saturation S—defined as the fraction of total receptors that are occupied (i.e. $S = [LR]/([LR]+[R])$)–exceeds 50% at the origin (the boundary between the production region and the rest of the domain), shown in (Figure S10D).

The reason for this is that morphogen decay is a function of *free* receptor level, and saturation amounts to lowering free receptor level. Thus, a gradient can, in principle, extend its apparent decay length simply by saturating receptors, but there are two reasons why this regime is likely to be un-biological. First, in this regime gradients adopt sigmoidal shapes, and such shapes are not observed in any known morphogen system. Second, a consequence of operating in this regime is that gradient position becomes extremely sensitive to small changes in the rate of morphogen production (Lander et al., 2009).

The plots in Figures S10C and S10D do not permit individual parameter sets—considered with and without feedback—to be compared against each other. We do this in Figure S10E, which shows the extent to which λ_{app} is increased by feedback. Notice that, when λ_{app}^{noFB} is less than half the value of λ_0, the improvement in λ_{app} that comes from feedback is always modest. This is because, in this regime, gradient shape is close to linear even in the absence of feedback, and thus both the feedback and non-feedback case display true source-sink scaling. However, once λ_{app}^{noFB} is on the order of λ_0 or larger, the improvement in λ_{app} due to feedback is much greater for almost all parameter sets: this is the pseudo-source-sink scaling regime, in which gradients remain quasilinear and scale automatically, even though the true sink is located many values of $\lambda_{intrinsic}$ away. In highly saturated regimes (red and yellow symbols), however, some of the feedback cases perform no better than the no-feedback cases, presumably because scaling due to saturation of receptors does not require feedback.

The Influence of Dimensionality on Source-Sink Scaling

Morphogen gradients often provide positional information along a single direction; in the wing disc, for example, the Dpp gradient patterns the anterioposterior (AP) axis. Even though biology happens in three dimensions, it is common to model morphogen gradients as reaction-diffusion systems in just this one dimension. This greatly simplifies analysis, but can introduce artifacts. Here we discuss one type of artifact that arises when wing discs are small, and can affect the shapes of gradients produced by the mathematical model described above.

In multiple dimensions, the steady state form of a reaction-diffusion equation within a morphogen domain in which morphogen is not produced is:

$$0 = D\nabla^2 C - f(C) \qquad \text{(Equation 22)}$$

where C is morphogen concentration, the first term describes diffusion, and the second term stands for any intrinsic decay processes. We focus on the steady state here because, as described elsewhere, the dynamic results of the model developed here are quasi-steady state (e.g. increasing or decreasing all rate constants proportionately has little effect on the model output).

If decay is linear, i.e. uniform in space and proportional to morphogen concentration, then this steady state equation becomes

$$0 = D\nabla^2 C - kC \qquad \text{(Equation 23)}$$

which may be written as

$$0 = \lambda_{intrinsic}^2 \nabla^2 C - C \qquad \text{(Equation 24)}$$

where $\lambda_{intrinsic}$ has its usual definition. This may be simplified further, if k is very small, i.e. if $\lambda_{intrinsic}$ is very large, to

$$0 = \nabla^2 C \qquad \text{(Equation 25)}$$

which is simply Fick's second law. This approximation is a good one whenever $\lambda_{intrinsic}$ is large compared with the size of the morphogen domain, a size that we will denote as x_{max}. In the model developed here, that condition applies to the very smallest disks, i.e. during the earliest simulation times.

In one dimension, Equation 25 becomes $0 = C''(x)$, which solves to a straight line. If the boundary conditions are such that there is a source at one end (x=0) and a sink at the other (x=x_{max}), then the equation of the line is

$$C = C_0\left(1 - \frac{x}{x_{max}}\right) \qquad \text{(Equation 26)}$$

where C_0 means concentration at x=0. We can see that such a gradient scales perfectly because the effects of multiplying x_{max} by any factor are exactly canceled by multiplying x by the same factor. This is the basis for the statement that purely "source-sink" gradients scale "automatically".

The more general one-dimensional form, Equation 24 also has an exact solution for the same boundary conditions, which is

$$C = C_0 \operatorname{csch}\frac{x_{max}}{\lambda_{intrinsic}} \sinh\frac{x_{max} - x}{\lambda_{intrinsic}}. \qquad \text{(Equation 27)}$$

When $\lambda_{intrinsic} >> x_{max}$, Equation 27 reduces to Equation 26. In contrast, when $\lambda_{intrinsic} << x_{max}$, Equation 27 reduces to

$$C = C_0 e^{-\frac{x}{\lambda_{intrinsic}}}. \quad \text{(Equation 28)}$$

This form does not scale at all, because C is completely independent of x_{max}. These observations tell us that, in a one-dimensional system with source-sink boundary conditions, linear shape always means automatic scaling (and vice versa), whereas exponential shape always means no scaling (and vice versa).

In the mathematical model described above, we see linear Dpp gradient shapes during the earliest stages of disc growth (until posterior compartment sizes reach about 20 μm), consistent with simple source-sink scaling due to the relatively small size of x_{max}. As required by Equation 26, these shapes are not only linear, but also extend all the way from source to the location of the sink (x_{max}), which in the model is taken to be the edge of the posterior compartment (the justification for this will become clear shortly). The model therefore makes the prediction that Dpp gradient shapes in the posterior compartments of the very smallest discs should be linear and extend from the Dpp source to the posterior disc edge.

In practice, assessing whether pMad gradient shapes are better fit by lines or exponential is not possible when discs are small, due to the noisiness of measurements, the rather small dynamic range over which pMad can be quantified by immunofluorescence, and the need to subtract unknown amounts of background fluorescence. Consider, for example, the pMad intensity data shown in the left panel of Figure S11A. Depending on the amount of background fluorescence one subtracts, one could fit the data reasonably well with a declining exponential shape (middle panel) or a straight line (right panel). However, if one does fit the data with a line, that line will not extend to the compartment edge (in the panel at right, that line intersects the background at a location only about a third of the way to the end of the domain.

On the face of it, this would appear to be an example of a strong disagreement between the model and the data: observed gradient shapes in small discs are either not linear, or do not extend far enough toward the compartment edge to fit the model. On closer examination, however, it turns out that this disagreement is most likely an artifact of the fact that the model is one dimensional, and thus ignores the dorsoventral (DV) and apicobasal (AB, i.e. cross-sectional) dimensions. Neglect of the DV direction is usually justified by the fact that the Dpp source is a long rectangle oriented parallel to the DV axis; if the rectangle is sufficiently long, and one keeps one's observations far enough away from its edges, then it is reasonable to expect that Dpp concentrations along the AP direction should be independent of DV position.

The greater problem arises with the AB dimension (for simplicity we will call this the "z" dimension, to contrast it with the "x" that we have been using to represent the AP axis). The impact of ignoring z is not widely discussed in the literature, possibly because there has been some uncertainty about the actual cell biological space in which Dpp diffuses and acts: the luminal space above columnar cells, or the basolateral space between columnar cells. If Dpp diffuses in the lumen, a thin space bounded on both sides by tight junctions, then it is probably safe to ignore z. But recent evidence strongly supports the view that, in the wing disc, Dpp's function is mediated almost exclusively by molecules diffusing in the basolateral space (Harmansa et al., 2017), a result also in agreement with observations that freely diffusing Dpp can be observed directly in that space by fluorescence correlation spectroscopy (Zhou et al., 2012). The basolateral space is bounded by tight junctions at one end (the apical surface), but only by a basement membrane at other end. Basement membranes are structures that pose no barrier to diffusion (Dowd et al., 1999). As diagrammed in Figure S11B (in which the basement membrane of the posterior columnar cells is highlighted in red), a continual "leakage" of Dpp out of discs through the basement membrane into the surrounding hemolymph is to be expected. In fact, recent evidence argues that delivery of Dpp from discs, via the hemolymph, to the rest of the larva is considerable during larval development (Setiawan et al., 2018).

How might such leakage alter morphogen gradient shapes when measured in the AP dimension? A general treatment of this problem can be found in (Lander et al., 2011), but more useful here is a discussion of the specific case when $\lambda_{intrinsic}$ is large (the scenario that, in the model, applies to the smallest discs). In that case, steady state shapes are determined by Equation 25. Because C is now a function of two dimensions, x and z, that equation no longer always solves to a straight line. As usual, the solution depends on the boundary conditions, which now must be specified in both x and z direction. In the x-direction, we choose a constant-value condition at x=0 simply to represent that the morphogen domain abuts a source at that location. We choose a zero-value (sink) condition at x=x_{max}, the posterior edge of the disc because, as we see in the Figure S11B, the basement membrane curves around at the edge of the disc, so that Dpp reaching that location is free to exit into the hemolymph (which, being a well-stirred compartment, quickly carries the Dpp away). In the z-direction, we also place a zero-value (sink) condition at z=0 (the basal surface of the disc), for the same reason. At the apical surface (z=z_{max}), we place a "zero-flux" boundary condition, to capture the presence of tight junctions that block the escape of molecules diffusing in basolateral space. Together, these conditions specify the two-dimensional model diagrammed in Figure S11C.

Due to symmetry considerations, this problem can be seen as simply the lower half of the problem in Figure S11D, which has only value (Dirichlet) boundary conditions, and for which a solution is well known (Bergman et al., 2011). Specifically, the steady state solution can be represented as the infinite sum:

$$C(x,z) = C_0 \sum_{n=1}^{\infty} \left(\frac{2\left(1+(-1)^{n+1}\right)}{n\pi} \sin\left(\frac{n\pi z}{2z_{max}}\right) \operatorname{csch}\left(\frac{n\pi x_{max}}{2z_{max}}\right) \sinh\left(\frac{n\pi(x_{max}-x)}{2z_{max}}\right) \right) \quad \text{(Equation 29)}$$

To see how this shape would appear to an observer focusing only on the AP plane, we may average over all z from z=0 to z=zmax, to get the following form

$$C(x) = C_0 \sum_{n=1}^{\infty} \left(\frac{\sin\left(\left(n-\frac{1}{2}\right)\frac{\pi}{2}\right)}{\left(n-\frac{1}{2}\right)\frac{\pi}{2}} \operatorname{csch}\left(\frac{\left(n-\frac{1}{2}\right)\pi x_{max}}{z_{max}}\right) \sinh\left(\frac{\left(n-\frac{1}{2}\right)\pi(x_{max}-x)}{z_{max}}\right)\right) \quad \text{(Equation 30)}$$

The result here is a sum of terms each of which has the form

$$\frac{1}{2\sqrt{2}a(n)} \operatorname{csch}\frac{x_{max}}{\lambda(n)} \sinh\frac{x_{max}-x}{\lambda(n)}. \quad \text{(Equation 31)}$$

With $a(n) = \pi, 3\pi, -5\pi, -7\pi, 11\pi, 13\pi, -15\pi\ldots$ and $\lambda(n) = \frac{2z_{max}}{\pi}, \frac{2z_{max}}{3\pi}, \frac{2z_{max}}{5\pi}, \frac{2z_{max}}{7\pi}\ldots$

Except for x near 0, the result is reasonably well approximated by the first term of the sum, i.e.

$$\frac{C_0}{2\sqrt{2}} \operatorname{csch}\frac{x_{max}}{\frac{2}{\pi}z_{max}} \sinh\frac{(x_{max}-x)}{\frac{2}{\pi}z_{max}} \quad \text{(Equation 32)}$$

Except for the leading constant, this form exactly matches Equation 27, with 2πzmax replacing $\lambda_{intrinsic}$. Thus, the shape of the morphogen gradient in the AP direction will be governed by the relationship between 2πzmax and x_{max}. At one extreme, where 2πzmax $\gg$ xmax, it will be a straight line from source to x_{max}. At the other extreme, where 2πzmax $\ll$ xmax, it will approach a declining exponential. Strikingly, however, regardless of the shape of the gradient, it will scale automatically in response to changes in x_{max}, provided that changes in x_{max} are always accompanied by proportional changes in z_{max}, i.e. if disc growth is isotropic. This can be seen directly from Equation 32: the effects of multiplying both x_{max} and z_{max} by any factor are exactly canceled by multiplying x by the same factor.

In summary, when morphogen gradients form under conditions of low intrinsic decay ($\lambda_{intrinsic} >> x_{max}$), and the morphogen domain is growing isotropically, we should expect to observe the same kind of automatic scaling that one-dimensional models predict, but we should not expect to see linear gradient shapes, especially if z_{max} is small compared with x_{max}. Measurements from confocal images indicate that, during disc growth, z_{max} is always small compared with x_{max}, implying that observed gradient shapes during automatic, source-sink scaling should actually be quasi-exponential, and not linear. As can be seen from Figure S11A, this prediction is consistent with our observations.

Does this mean the one-dimensional model needs to be discarded in favor of a more complicated two (or even three)-dimensional one? Not necessarily. Although the model predicts incorrect shapes during the earliest phases of disc growth, it does capture scaling behavior correctly, including the loss of scaling that takes place when discs grow large enough that the condition $\lambda_{intrinsic} >> x_{max}$ starts to fail. In the two-dimensional model, the analytical solution for gradient shape under these conditions is more complicated (see (Lander et al., 2011)), but scaling eventually fails in the same way, at the same time, and for the same reasons. Moreover, it is straightforward to show that when discs grow sufficiently big that $\lambda_{ntrinsic} << z_{max}$, shape in the AP direction becomes effectively uncoupled from AB shape (i.e., the z-direction), meaning that the results of the one-dimensional model eventually closely approximate the two-dimensional one in all respects. Overall, then, accounting for the AB direction imposes a relatively modest correction on the one-dimensional model, which is limited to early periods of disc growth.

QUANTIFICATION AND STATISTICAL ANALYSIS

Image Analysis

Measurements of pMad staining intensity were performed using Fiji. Images were quantified by scanning along a straight line starting at the anteroposterior (A/P) boundary and ending at the edge of the wing pouch, parallel to the anterior-posterior axis, with about 20% dorsal offset from dorsoventral (D/V) boundary. Both pMad and Ptc fluorescence intensity profiles were extracted along the line. Automated algorithms were developed in Wolfram *Mathematica* to detect the location of the A/P compartment boundary (the edge of Dpp production region) using these fluorescence intensity profiles. To make sure that the locations of the A/P compartment boundaries determined by the automated algorithms were accurate, we manually checked the intensity profiles of each wing disc, and made corrections if necessary. Posterior compartment size was quantified by following a segmented line along the Wg staining at the D/V boundary (starting from the A/P boundary and ending at the edge of the wing pouch), and measuring the length of the line. To obtain a value of λ_{app}, the pMad profile was fitted to the function $y(x) = a\, e^{-x/\lambda} + b$, where $\lambda = \lambda_{app}$ and b is background intensity, using the ''NonlinearModelFit'' (non-linear fitting function) in Wolfram *Mathematica*. Data were statistically analyzed using Microsoft Excel and Wolfram *Mathematica*. Similar methods were used to analyze GFP-Pent and DppDendra2 profiles. All statistical details of experiments can be found in the figure legends. n represents number of discs. Error bars represent SEM in all figures.

Fitting Scaling Dynamics

Inspection of pMad gradients at multiple stages of development suggested that λ_{app} increases more or less linearly with disc size until a threshold size is reached; after that, λ_{app} either remains constant or increases linearly but at a slower rate. To quantify this behavior

with a minimum of parameters, we identified a general functional form that transitions sharply from one constant slope to another at a particular point. Briefly, the function is the solution to the differential equation $f'(x) = (b\text{-}a)/(1+(x/c)^n)+a$, where c represents the switching point, b is the slope when $x<<c$ and a is the slope when $x>>c$ (the solution can be represented explicitly as a hypergeometric function). The Hill coefficient, n, controls the sharpness of the switching at the turning point c, and for sufficiently large values of n has almost no influence on the quality of the fit of this function to the data. In the plots in Figures 4 and 5, fitting was carried out using ''NonlinearModelFit'' in Wolfram *Mathematica*, and a value of n=9.